FINITE ELEMENT METHODS FOR MECHANICAL ENGINEERS

SARAH BARDIN

ABSTRACT. We present, motivate, and exercise the Finite Element Method through analysis of thermal and structural behavior of several related systems. In Chapter 1, we examine the Rayleigh-Ritz method, a numerical method of solving physical boundary value problems that can be expressed as matrix differential equations. We discussed the method through two illustrative examples, quasi-1D heat conduction in a conical frustum insulated on the lateral surfaces with heat flux and heat transfer coefficient boundary conditions and a right-cylinder thermal fin with temperature and zero-flux boundary conditions. In Chapter 2, we examine the Finite Element Method for 1D SPD boundary value problems. We consider again the first two models of Chapter 1, and additionally a right-cylinder with heat transfer coefficient boundary conditions on the left and right surfaces. In Chapter 3, we add time dependence into our study of FEM through examination of the 1D transient heat equation. Using a finite difference method, we discretized the temporal components of our boundary value problem. In Chapter 4, we shift our focus to application of FEM to structural analysis, specifically beam bending. We introduce eigenproblems through study of the design and tuning of a xylophone bar. Finally, in Chapter 5, through similar analysis to that of Chapter 4, we examine buckling and, in particular, self-buckling.

1. The Rayleigh-Ritz Method

1.1. Model I: Neumann/Robin Boundary Conditions.

For the first model, we consider quasi-1D heat conduction in a conical frustum insulated on the lateral surfaces with heat flux and heat transfer coefficient boundary conditions on the left and right surfaces, respectively. The equations and boundary conditions are given by

$$-k\frac{d}{dx}\left(\pi R_0^2\left(1+\beta\frac{x}{L}\right)^2\frac{du}{dx}\right)=0 \text{ in } \Omega\ , \tag{1}$$

$$k\frac{du}{dx}=-q_1 \text{ on } \Gamma_1\ , \tag{2}$$

$$-k\frac{du}{dx}=\eta_2(u-u_\infty) \text{ on } \Gamma_2\ , \tag{3}$$

where $\Omega=(0,L)$, $\Gamma_1=\{0\}$, $\Gamma_2=\{L\}$, k, R_0, L, and η_2 are positive constants, β is a nonnegative constant, and q_1, u_∞ are constants. The exact solution is given by

$$u=u_\infty+\frac{q_1L}{k}\left(\frac{1+\beta+\frac{k}{\eta_2 L}}{(1+\beta)^2}-\frac{(\frac{x}{L})}{1+\beta(\frac{x}{L})}\right). \tag{4}$$

We introduce the candidate function $w(x)$ where $\int_0^L w^2dx<\infty$ and $\int_0^L(\frac{dw}{dx})^2dx<\infty$. We then construct the energy functional $\Pi(w)\in\mathbb{R}$ such that the exact solution,

$u = \text{argmin}_{w \in X} \Pi(w)$. To derive the energy functional, (1) is multiplied by a test function $v \in X$ and integrated over the domain to obtain

$$\int_0^L \left[\frac{d}{dx} \left(-k\pi R_0^2 \left(1 + \beta \frac{x}{L} \right)^2 \frac{du}{dx} \right) \right] v dx = 0. \tag{5}$$

We then apply the Laplacian variant of Green's First Identity to the first term of the integral on the left-hand side of (5) to obtain

$$\int_0^L k\pi R_0^2 \left(1 + \beta \frac{x}{L} \right)^2 \frac{du}{dx} \frac{dv}{dx} dx - k\pi R_0^2 \left(1 + \beta \frac{x}{L} \right)^2 \frac{du}{dx} v \Bigg|_0^L = 0. \tag{6}$$

Substituting boundary conditions into (6) yields

$$\int_0^L k \left(1 + \beta \frac{x}{L} \right)^2 \frac{du}{dx} \frac{dv}{dx} dx + \eta_2 (1+\beta)^2 (u(L) - u_\infty) v(L) - q_1 v(0) = 0. \tag{7}$$

Matching (7) to $a(u, v) = f(v)$, $\forall v \in X$, we can identify bilinear form $a : H^1(\Omega) \times H^1(\Omega) \to \mathbb{R}$

$$a(w, v) = \int_0^L k \left(1 + \beta \frac{x}{L} \right)^2 \frac{dw}{dx} \frac{dv}{dx} dx + \eta_2 (1+\beta)^2 w(L) v(L), \tag{8}$$

and linear form $f : H^1(\Omega) \to \mathbb{R}$

$$f(v) = \eta_2 (1+\beta)^2 u_\infty v(L) + q_1 v(0). \tag{9}$$

Finally, we apply $\Pi(w) = \frac{1}{2} a(w, w) - f(w)$ to obtain the energy functional

$$\begin{aligned} \Pi(w) = \frac{1}{2} \left(\int_0^L k \left(1 + \beta \frac{x}{L} \right)^2 \left(\frac{dw}{dx} \right)^2 dx + \eta_2 (1+\beta)^2 w(L)^2 \right) \\ - \left(\eta_2 (1+\beta)^2 u_\infty w(L) + q_1 w(0) \right). \end{aligned} \tag{10}$$

From the energy functional, $\Pi(w)$, we can specify the $n^{RR} \times n^{RR}$ system of linear equations, $\underline{A}\ \underline{\alpha}^{RR} = \underline{F}$, which must be satisfied by the Rayleigh-Ritz coefficients $\underline{\alpha}^{RR} \in \mathbb{R}^{n^{RR}}$. For this model, we consider the Rayleigh-Ritz approximation

$$u^{RR}(x) = \sum_{i=1}^{n^{RR}} \alpha_i^{RR} \psi_i(x). \tag{11}$$

Substituting (11) into (10) yields the algebraic form of energy

$$\begin{aligned}\Pi\left(\sum_{i=1}^{n^{RR}}\alpha_i^{RR}\psi_i(x)\right) = \frac{1}{2}\Bigg[\int_0^L k\left(1+\beta\frac{x}{L}\right)^2\left(\sum_{i=1}^{n^{RR}}\alpha_i^{RR}\frac{d\psi_i}{dx}\right)\left(\sum_{j=1}^{n^{RR}}\alpha_j^{RR}\frac{d\psi_j}{dx}\right)dx \\ + \eta_2(1+\beta)^2\left(\sum_{i=1}^{n^{RR}}\alpha_i^{RR}\psi_i(L)\right)\left(\sum_{j=1}^{n^{RR}}\alpha_j^{RR}\psi_j(L)\right)\Bigg] \\ - \Bigg[\eta_2(1+\beta)^2u_\infty\left(\sum_{i=1}^{n^{RR}}\alpha_i^{RR}\psi_i(L)\right) \\ + q_1\left(\sum_{i=1}^{n^{RR}}\alpha_i^{RR}\psi_i(0)\right)\Bigg].\end{aligned} \tag{12}$$

From (12) we can construct matrices $\underline{A} \in \mathbb{R}^{n^{RR}\times n^{RR}}$

$$A_{ij} = \int_0^L k\left(1+\beta\frac{x}{L}\right)^2\frac{d\psi_i}{dx}\frac{d\psi_j}{dx}dx + \eta_2(1+\beta)^2\psi_i(L)\psi_j(L), \tag{13}$$

and $\underline{F} \in \mathbb{R}^{n^{RR}}$

$$F_i = \eta_2(1+\beta)^2u_\infty\psi_i(L) + q_1\psi_i(0), \tag{14}$$

such that (13) can be reframed as

$$\Pi\left(\sum_{i=1}^{n^{RR}}\alpha_i^{RR}\psi_i(x)\right) = \frac{1}{2}\underline{\alpha}^T\underline{A}\underline{\alpha} - \underline{\alpha}^T\underline{F} = Q_\Pi(\underline{\alpha}). \tag{15}$$

Our Rayleigh-Ritz minimization problem is constructed such that $\underline{\alpha}^{RR}$ minimizes $Q_\Pi(\underline{\alpha})$. From (15) we can derive the first order condition

$$\frac{\partial Q_\pi}{\partial\alpha_k}(\underline{\alpha}^{RR}) = 0,\ \underline{A\alpha}^{RR} = \underline{F}, \tag{16}$$

and the second order condition

$$Q_\pi(\underline{\alpha}^{RR} + \underline{z}) > Q_\pi(\underline{\alpha}^{RR}),\ \forall\underline{z} \in \mathbb{R}^{n^{RR}}. \tag{17}$$

After constructing the model, we considered two sets of basis functions:
`exactinclude`: $n^{RR} = 2$ for $\psi_1(x) = u(x)$ and $\psi_2(x) = x$
`conslinquad` : $n^{RR} = 1$ for $\psi_1(x) = 1$
$n^{RR} = 2$ for $\psi_1(x) = 1$ and $\psi_2(x) = x$
$n^{RR} = 3$ for $\psi_1(x) = 1$, $\psi_2(x) = x$, and $\psi_3(x) = x^2$

The Rayleigh-Ritz method returns the combination of chosen basis functions that best approximates the true solution. To verify that the implementation is correct we first consider the `exactinclude` case. Given the exact solution as the first basis function, $\psi_1(x)$, the Rayleigh-Ritz method returns a value of 1 for α_1^{RR} and 0 for all other coefficients. Any combination of the exact solution and another basis function would result in a worse approximation.

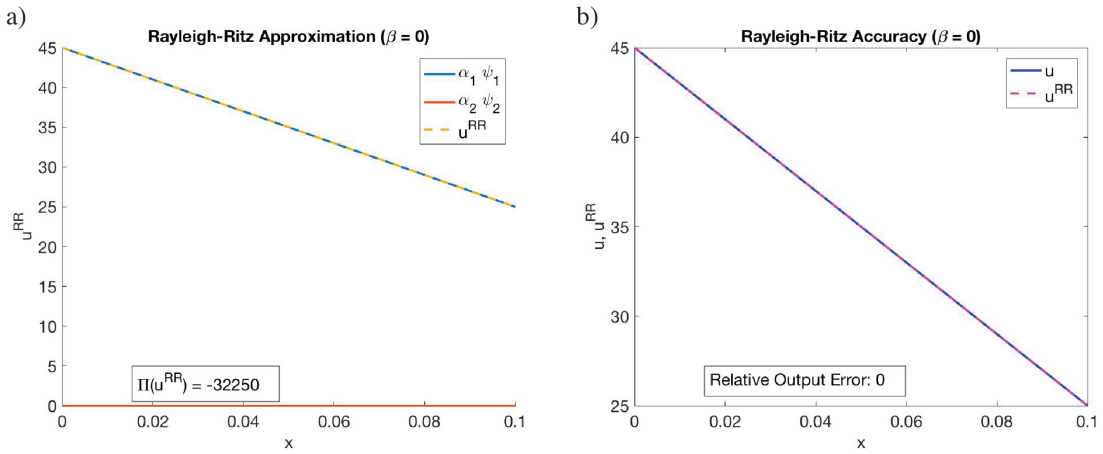

FIGURE 1. (a) The Rayleigh-Ritz approximation, u^{RR}, given basis functions $\psi_1(x) = u(x)$ and $\psi_2(x) = x$. (b) The relative output error in the E_{III} norm between the approximation, u^{RR}, and the exact solution, u, is zero.

The results show visually that the Rayleigh-Ritz approximation, u^{RR}, is not taking a linear combination of ψ_1 and ψ_2 (Figure 1a). More specifically, ψ_2 provides no contribution to u^{RR}. The relative output error in the E_{III} norm is zero, as expected (Figure 1b).

Next, we consider the `constlinquad` case. For a value of $\beta = 0$, the exact solution (4) is a linear function of x.

$$u = u_\infty + \frac{q_1 L}{k}\left(1 + \frac{k}{\eta_2 L} - \frac{x}{L}\right). \tag{18}$$

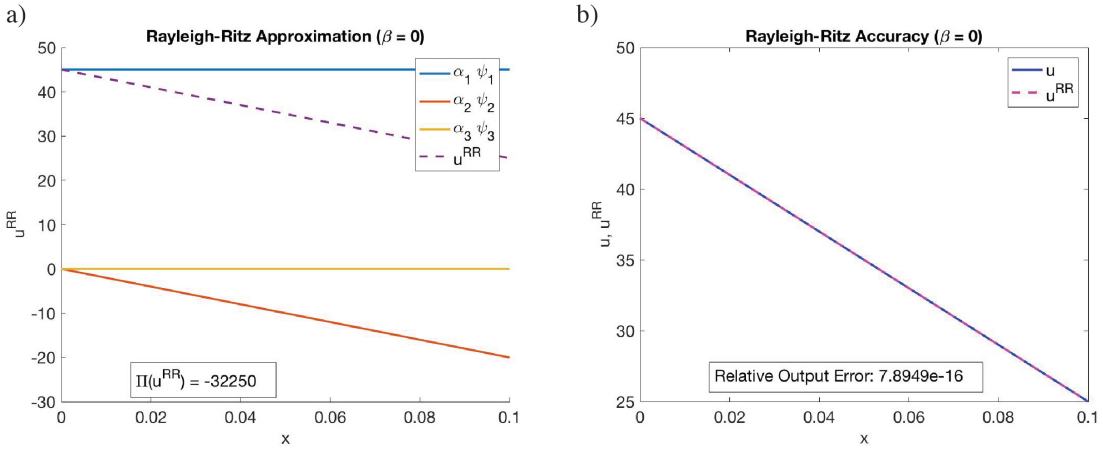

FIGURE 2. (a) The Rayleigh-Ritz approximation, u^{RR}, given basis functions $\psi_1(x) = 1$, $\psi_2(x) = x$, and $\psi_3(x) = x^2$. (b) The relative output error in the E_{III} norm between the approximation, u^{RR}, and the exact solution, u, is approximately zero.

Given a constant, linear, and quadratic basis function, the results show that the Rayleigh-Ritz approximation returns a combination of just the constant and linear

basis functions (Figure 2a). Because the exact solution is a linear function of x, a linear combination including the quadratic function would result in a worse approximation. The corresponding α^{RR} values were $\alpha_1^{RR} = 45$, $\alpha_2^{RR} = -200$, and $\alpha_3^{RR} = 0$, confirming that the third quadratic basis function does not contribute to u_{RR}. The relative output error, in the E_{III} norm, between the approximation and the exact solution is approximately zero, as a linear exact solution can be well approximated with constant and linear basis functions (Figure 2b).

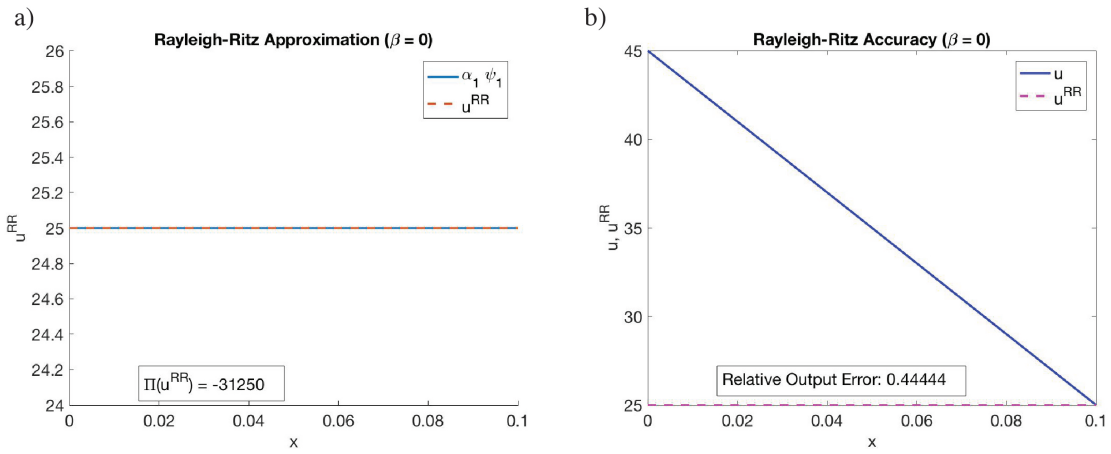

FIGURE 3. (a) The Rayleigh-Ritz approximation, u^{RR}, given a single basis function $\psi_1(x) = 1$. (b) The relative output error in the E_{III} norm between the approximation, u^{RR}, and the exact solution, u, is 0.44.

For the case of a single basis function ψ_1 the performance of the Rayleigh-Ritz model is far worse than that of the previous case of three basis functions (Figure 3b). This provides some confidence that the implementation is correct because the error from the approximation given one basis function, ψ_1, can not be strictly smaller than the error from an approximation given the same basis function, ψ_1, and additional basis functions, ψ_i. The large relative output error in the E_{III} norm is also expected in the sense that we are trying to approximate a linear solution with a constant function (Figure 3).

Comparison of the results of `exactinclude` and `constlinquad` shows that the relative output error of `exactinclude` is always less than or equal to that of `constlinquad`. In other words, it is not possible for `constlinquad` to outperform `exactinclude` because the exact solution, included as a basis function, is the minimizer of our energy functional.

Finally, we examine the effect of our chosen value of β on the relative output error of our model.
For small values of β, the relative output error in the E_{III} norm scales with β (Figure 4abc). This is expected as increases in β alter the shape of the exact solution curve such that it is harder to approximate with just a constant, linear, and quadratic function. Specifically, the curve is no longer linear and instead exhibits more extreme slopes for higher and lower values of x (Figure 4). Outside the range of small, more practical, values of β, the relative output error begins to decrease. This is because for high values of β the curve develops a much longer tail on the right. By examination

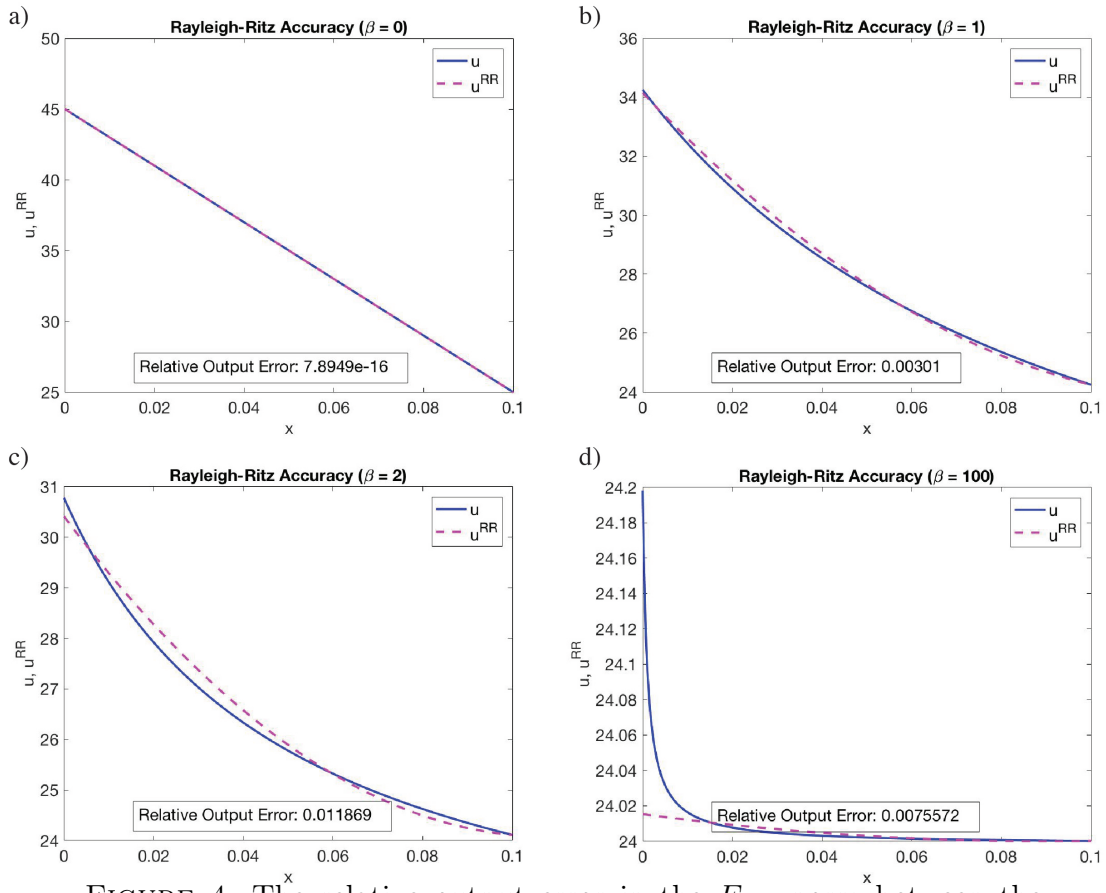

FIGURE 4. The relative output error in the E_{III} norm between the Rayleigh-Ritz approximation, u^{RR}, and the exact solution, u, for β values of 0 (a), 1 (b), 2 (c), and 100 (d). The chosen basis functions were $\psi_1(x) = 1$, $\psi_2(x) = x$, and $\psi_3(x) = x^2$.

of the exact solution (4), we can see that as $\beta \to \infty$, $u \to u_\infty$, a constant value. The smaller relative output error for large values of β is a consequence of this behavior: as the exact solution approaches a constant value, we are able to better approximate it given a constant, linear, and quadratic basis function.

1.2. **Model II: Dirichlet Boundary Conditions.**

For second model, we consider a right-cylinder thermal fin with temperature and zero-flux boundary conditions on the left and right surfaces, respectively. The equations and boundary conditions are given by

$$-kA_{cs}\frac{d^2u}{dx^2} + \eta_3 P_{cs}(u - u_\infty) = 0 \text{ in } \Omega \ , \tag{19}$$

$$u = u_{\Gamma_1} \text{ on } \Gamma_1 \ , \tag{20}$$

$$-k\frac{du}{dx} = 0 \text{ on } \Gamma_2 \ , \tag{21}$$

where $\Omega = (0, L)$, $\Gamma_1 = \{0\}$, $\Gamma_2 = \{L\}$, k, A_{cs}, P_{cs}, and η_3 are positive constants, and u_{Γ_1} is a constant. The exact solution to this problem is given by

$$u = u_\infty + (u_{\Gamma_1} - u_\infty)\frac{\cosh\left(\sqrt{\mu_0}\left(1 - \frac{x}{L}\right)\right)}{\cosh(\sqrt{\mu_0})}, \tag{22}$$

where $\mu_0 = \frac{\eta_3 P_{cs} L^2}{k A_{cs}}$.

We introduce the candidate function, $w(x)$, where $\int_0^L w^2 dx < \infty$, $\int_0^L (\frac{dw}{dx})^2 dx < \infty$, and $w|_{\Gamma_1} (= w(0)) = u_{\Gamma_1}$. For the Dirichlet boundary condition case, we also introduce an admissible function, $v(x)$, where $\int_0^L v^2 dx < \infty$, $\int_0^L (\frac{dv}{dx})^2 dx < \infty$, and $v|_{\Gamma_1} (= v(0)) = 0$. Finally, as in the first model, we construct an energy functional $\Pi(w) \in \mathbb{R}$ such that the exact solution, $u = \text{argmin}_{w \in X} \Pi(w)$. To derive the energy functional, (19) is multiplied by a test function $v \in X$ and integrated over the domain to obtain

$$\int_0^L \left[\frac{d}{dx} \left(-kA_{cs} \frac{du}{dx} \right) + \eta_3 P_{cs} (u - u_\infty) \right] v dx = 0. \tag{23}$$

We then apply the Laplacian variant of Green's First Identity to the first term of the integral on the left-hand side of (23) to obtain

$$\int_0^L kA_{cs} \frac{du}{dx} \frac{dv}{dx} dx + \int_0^L \eta_3 P_{cs} (u - u_\infty) v dx - kA_{cs} \frac{du}{dx} v \Big|_0^L = 0. \tag{24}$$

Substituting boundary conditions into (24) yields

$$\int_0^L kA_{cs} \frac{du}{dx} \frac{dv}{dx} dx + \int_0^L \eta_3 P_{cs} u v dx - \int_0^L \eta_3 P_{cs} u_\infty v dx = 0. \tag{25}$$

Matching (25) to $a(u, v) = f(v)$, $\forall v \in X$, we can identify bilinear form $a : H^1(\Omega) \times H^1(\Omega) \to \mathbb{R}$

$$a(w, v) = \int_0^L kA_{cs} \frac{dw}{dx} \frac{dv}{dx} dx + \int_0^L \eta_3 P_{cs} w v dx, \tag{26}$$

and linear form $f : H^1(\Omega) \to \mathbb{R}$

$$f(v) = \int_0^L \eta_3 P_{cs} u_\infty v dx. \tag{27}$$

Finally, we apply $\Pi(w) = \frac{1}{2} a(w, w) - f(w)$ to obtain the energy functional

$$\Pi(w) = \frac{1}{2} \left(\int_0^L \left[kA_{cs} \left(\frac{dw}{dx} \right)^2 + \eta_3 P_{cs} w^2 \right] dx \right) - \int_0^L \eta_3 P_{cs} u_\infty w dx. \tag{28}$$

From the energy functional, $\Pi(w)$, we can specify the $n^{RR+1} \times n^{RR+1}$ system of linear equations, $\underline{\widetilde{A}}\, \underline{\widetilde{\alpha}}^{RR} = \underline{\widetilde{F}}$, which must be satisfied by the Rayleigh-Ritz coefficients $\underline{\widetilde{\alpha}}^{RR} \in \{\mathbb{R}^{n^{RR+1}} | \widetilde{\alpha}_0 = u_{\Gamma_1}\}$. For this model, we consider the Rayleigh-Ritz approximation

$$u^{RR}(x) = \sum_{i=0}^{n^{RR}} \widetilde{\alpha}_i^{RR} \psi_i(x) = u_{\Gamma_1} \psi_0(x) + \sum_{i=1}^{n^{RR}} \alpha_i^{RR} \psi_i(x). \tag{29}$$

To account for Dirichlet boundary conditions our basis functions must satisfy $\psi_0(0) = 1$ and $\psi_i(0) = 0$ for $1 \leq i \leq n^{RR}$. Substituting (29) into (28) yields the algebraic

form of energy

$$\Pi\left(\sum_{i=0}^{n^{RR}}\alpha_i^{RR}\psi_i(x)\right) = \frac{1}{2}\int_0^L\left[kA_{cs}\left(\sum_{i=0}^{n^{RR}}\alpha_i^{RR}\frac{d\psi_i(x)}{dx}\right)\left(\sum_{j=0}^{n^{RR}}\alpha_j^{RR}\frac{d\psi_j(x)}{dx}\right)\right.$$
$$\left.+\eta_3 P_{cs}\left(\sum_{i=0}^{n^{RR}}\alpha_i^{RR}\psi_i(x)\right)\left(\sum_{j=0}^{n^{RR}}\alpha_j^{RR}\psi_j(x)\right)\right]dx\Bigg] \tag{30}$$
$$-\int_0^L \eta_3 P_{cs}u_\infty\left(\sum_{i=0}^{n^{RR}}\alpha_i^{RR}\psi_i(x)\right)dx.$$

From (30) we can construct matrices $\underline{\widetilde{A}} \in \mathbb{R}^{n^{RR+1}\times n^{RR+1}}$

$$\widetilde{A}_{ij} = \int_0^L\left[kA_{cs}\frac{d\psi_i}{dx}\frac{d\psi_j}{dx} + \eta_3 P_{cs}\psi_i(x)\psi_j(x)\right]dx, \tag{31}$$

and $\underline{\widetilde{F}} \in \mathbb{R}^{n^{RR}}$

$$\widetilde{F}_i = \int_0^L \eta_3 P_{cs}u_\infty\psi_i(x)dx, \tag{32}$$

such that (30) can be reframed as

$$\Pi\left(\sum_{i=1}^{n^{RR}}\alpha_i^{RR}\psi_i(x)\right) = \frac{1}{2}\underline{\widetilde{\alpha}}^T\underline{\widetilde{A}}\underline{\widetilde{\alpha}} - \underline{\widetilde{\alpha}}^T\underline{\widetilde{F}} = \widetilde{Q}_\Pi(\underline{\widetilde{\alpha}}). \tag{33}$$

After applying the standard Rayleigh-Ritz procedure, as seen in Model I, without regard to Dirichlet boundary conditions, we extract $\underline{A}$, $\underline{b}$, and $\underline{F}$, from $\underline{\widetilde{A}}$ and $\underline{\widetilde{F}}$. More specifically, we can rewrite $\widetilde{Q}_\Pi(\underline{\widetilde{\alpha}})$ as

$$\begin{aligned}\widetilde{Q}_\Pi(\underline{\widetilde{\alpha}}) &= \frac{1}{2}\widetilde{\alpha}_0 A_{00}\widetilde{\alpha}_0 - \widetilde{\alpha}_0\widetilde{F}_0 + \frac{1}{2}\underline{\alpha}^T\underline{A\alpha} + \underline{\alpha}^T\underline{b}\widetilde{\alpha}_0 - \underline{\alpha}^T\underline{F}\\ &= \widetilde{C} + \frac{1}{2}\underline{\alpha}^T\underline{A\alpha} - \underline{\alpha}^T(\underline{F} - u_{\Gamma_1}\underline{b})\end{aligned} \tag{34}$$

Our Rayleigh-Ritz minimization problem is now constructed such that $\underline{\widetilde{\alpha}}^{RR}$ minimizes $Q_\Pi(\underline{\widetilde{\alpha}})$. From (34) we can derive the first order condition

$$\underline{A\alpha}^{RR} = (\underline{F} - u_{\Gamma_1}\underline{b}) \tag{35}$$

Solving (35) yields $\underline{\alpha}^{RR}$ from which we can form $\underline{\widetilde{\alpha}}^{RR}$ by appending u_{Γ_1} as the first entry. Finally, we are able to evaluate $\Pi(u^{RR})$ from $\underline{\alpha}^{RR}$, $\underline{\widetilde{A}}$, $\underline{\widetilde{F}}$, similarly to Model I.

After constructing the model, we considered two sets of basis functions:
`exactinclude`: $\psi_0(x) = \frac{u(x)}{u_{\Gamma_1}}$; $n^{RR} = 1$ for $\psi_1(x) = x$
`conslinquad` :$\psi_0(x) = 1$; $n^{RR} = 1$ for $\psi_1(x) = x$
$n^{RR} = 2$ for $\psi_1(x) = x$ and $\psi_2(x) = x^2$

To verify that the implementation of this model is correct, we first consider the `exactinclude` case. Given the exact solution, normalized by u_{Γ_1}, as the first basis function, $\psi_0(x)$, the Rayleigh-Ritz method returns values of 0 for all coefficients except, $\widetilde{\alpha}_0^{RR} = u_{\Gamma_1}$. Unlike the first model, to verify the implementation is correct, we can not simply include the exact solution as one of the basis functions. Instead, we

have to divide $u(x)$ by u_{Γ_1} in our basis function because $\widetilde{\alpha}_0^{RR}$ takes on the value of u_{Γ_1}. Therefore, to obtain $u^{RR}(x) = u(x)$, the coefficient of u_{Γ_1} on $\psi_0(x)$ must be canceled out.

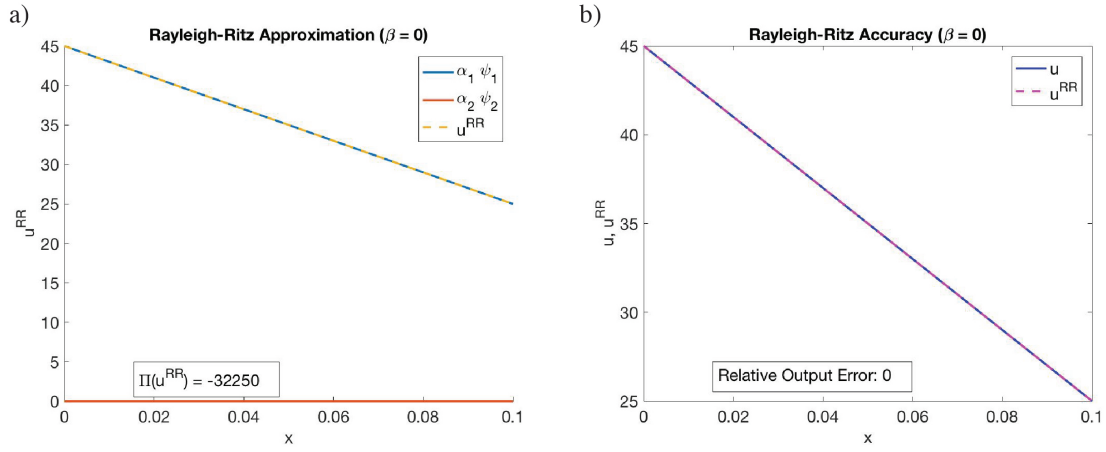

FIGURE 5. (a) The Rayleigh-Ritz approximation, u^{RR}, given basis functions $\psi_0(x) = \frac{u(x)}{u_{\Gamma_1}}$; $n^{RR} = 1$ for $\psi_1(x) = x$. Note, $\psi_1(x)$ in the image corresponds to $\psi_0(x)$ and so on. (b) The relative output error in the E_{III} norm between the approximation, u^{RR}, and the exact solution, u, is zero.

The results show visually that the Rayleigh-Ritz approximation, u^{RR}, is not taking a linear combination of ψ_0 and ψ_1, reaffirming our model (Figure 5a). More specifically, ψ_1 provides no contribution to u^{RR}. The relative output error in the E_{III} norm between the exact solution and the approximation is zero, as expected (Figure 5b).

Next, we consider the `constlinquad` case with $n^{RR} = 2$ and $\psi_0(x) = 1$

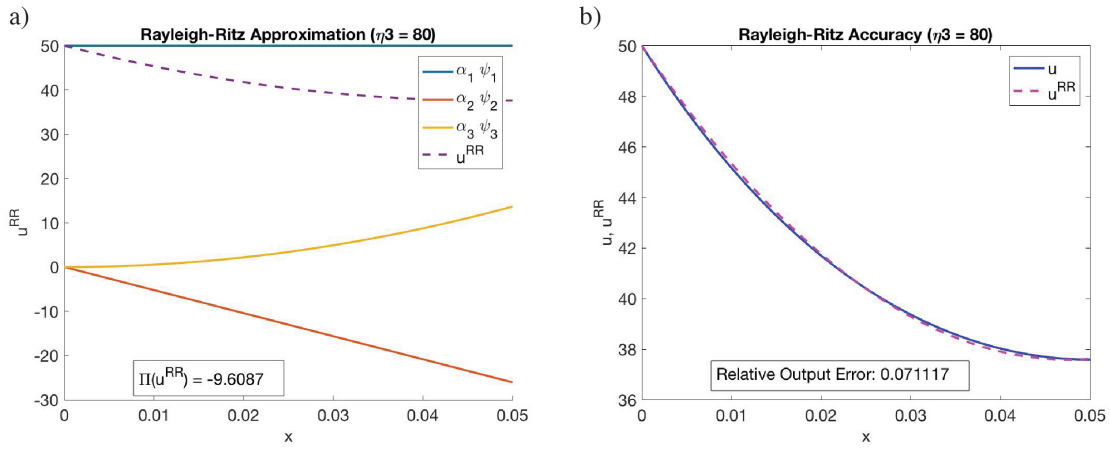

FIGURE 6. (a) The Rayleigh-Ritz approximation, u^{RR}, given basis functions $\psi_0(x) = 1$; $n^{RR} = 2$ for $\psi_1(x) = x$ and $\psi_2(x) = x^2$. Note, $\psi_1(x)$ in the image corresponds to $\psi_0(x)$ and so on. (b) The relative output error in the E_{III} norm between the approximation, u^{RR}, and the exact solution, u, is 0.07.

Given basis functions $\psi_1(x) = x$ and $\psi_2(x) = x^2$, the Rayleigh-Ritz approximation

returns $\widetilde{\alpha}^{RR}$ values of $\widetilde{\alpha}_1^{RR} = -520.8$ and $\widetilde{\alpha}_2^{RR} = -5465.2$. We can also confirm that the value of $\widetilde{\alpha}_0^{RR} = u_{\Gamma_1}$. The results show visually that the approximation, u^{RR}, is a linear combination of the linear and quadratic basis functions, along with ψ_0 (Figure 6a). The relative output error in the E_{III} norm between the approximation, u^{RR}, and the exact solution, u, is 0.07 (Figure 6b). This is larger than the relative output error for the `exactinclude` case, as expected, because we are not including the exact solution as a basis function.

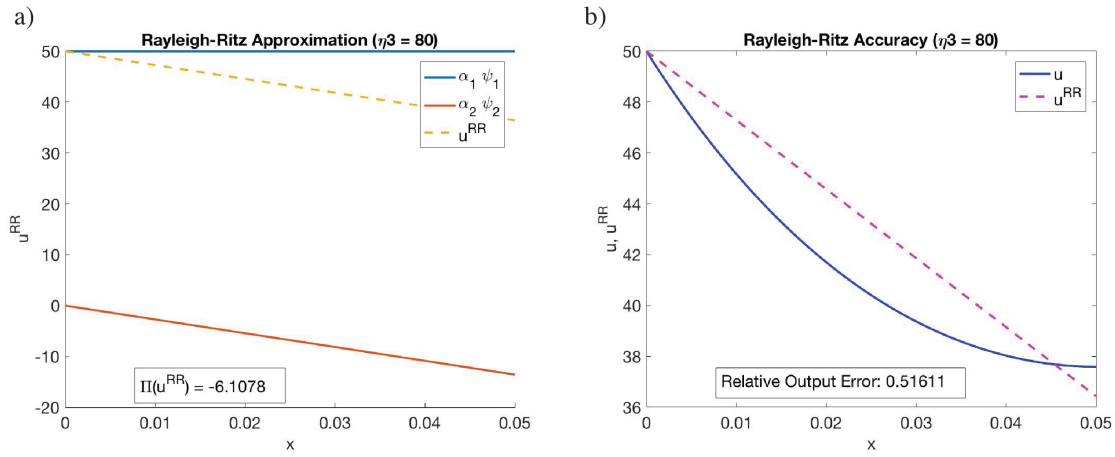

FIGURE 7. (a) The Rayleigh-Ritz approximation, u^{RR}, given two basis functions $\psi_0(x) = 1$; $n^{RR} = 1$ for $\psi_1(x) = x$. Note, $\psi_1(x)$ in the image corresponds to $\psi_0(x)$ and so on. (b) The relative output error in the E_{III} norm between the approximation, u^{RR}, and the exact solution, u, is 0.52.

For the case of two basis functions $\psi_0(x) = 1$ and $\psi_1(x) = x$ the performance of the Rayleigh-Ritz model is far worse than that of the previous case of three basis functions (Figure 7b). This provides some confidence that the implementation is correct because, like the first model, the relative output error in the E_{III} norm from the approximation given two basis functions, ψ_0 and ψ_1, can not be strictly smaller than the error from an approximation given the same two basis functions, ψ_0 and ψ_1, and additional basis functions, ψ_i. The large relative output error is also expected in the sense that we are trying to approximate a nonlinear exact solution with a linear basis function (Figure 7).

Identical to the first model, comparison of the results of `exactinclude` and `constlinquad` shows that the relative output error, in the E_{III} norm, of `exactinclude` is always less than or equal to that of `constlinquad`. In other words, it is not possible for `constlinquad` to outperform `exactinclude` because the exact solution, included as a basis function, is the minimizer of our energy functional.

Finally, we examine the effect of our chosen value of μ_0 on the relative output error of our model. We defined $\mu_0 = \frac{\eta_3 P_{cs} L^2}{k A_{cs}}$ and varied η_3 in the implementation.
From the results we can see that relative output error in the E_{III} norm scales with η_3, and subsequently, with μ_0. Similar to the effect of increasing β in model I, increasing μ_0 alters the exact solution curve such that it has a much longer tail and steeper initial slope. This change in shape makes it harder to approximate the solution with

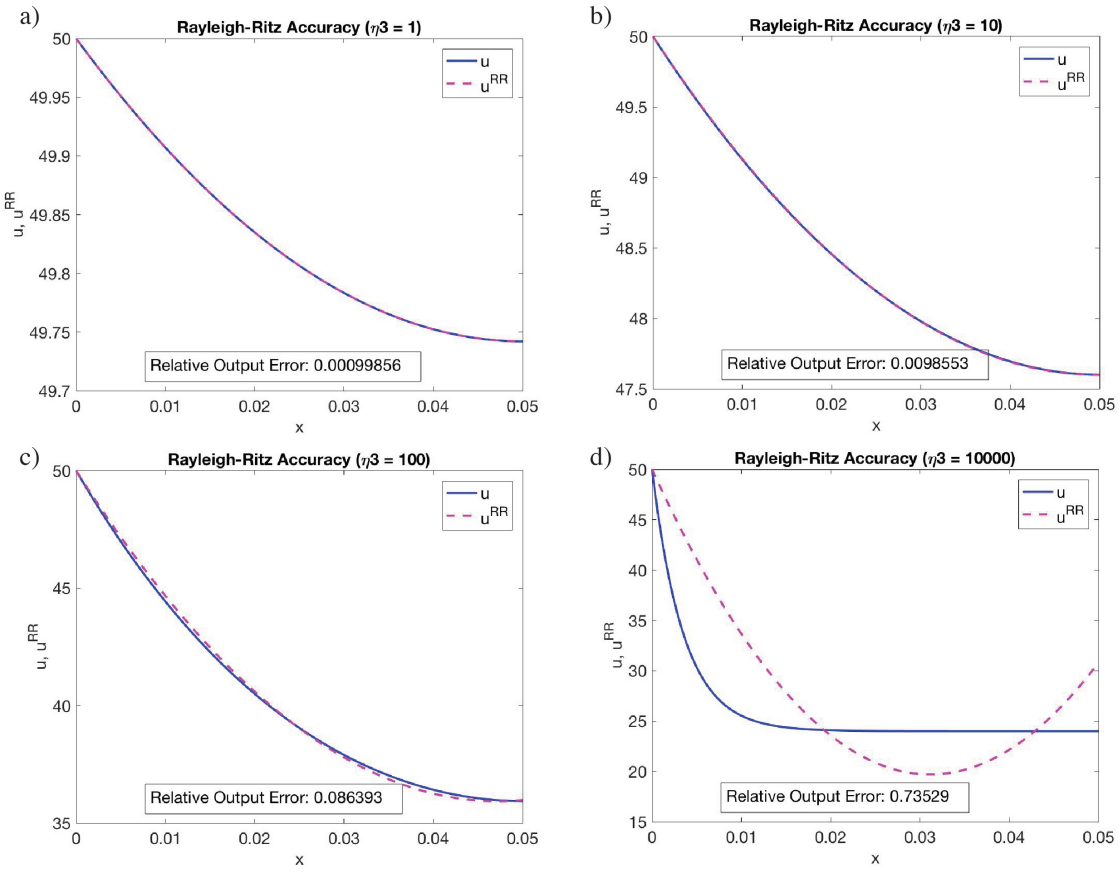

FIGURE 8. The relative error between the Rayleigh-Ritz approximation, u^{RR}, and the exact solution, u, for η_3 values of 1 (a), 10 (b), 100 (c), and 10000 (d). The chosen basis functions were $\psi_0(x) = 1$; $n^{RR} = 2$ for $\psi_1(x) = x$ and $\psi_2(x) = x^2$.

only constant, linear, and quadratic basis functions. Physically, as the curve takes on this shape it becomes representative of a long, over-designed fin, in which much of the length is not necessary.

2. The FE Method for 1D 2nd-Order SPD BVPs

In this chapter, we examine the FE Method for 1D 2nd-Order SPD BVPs through consideration of the first two models of Chapter 1, and an additional Neumann/Robin model.

2.1. **Model I: Neumann/Robin Boundary Conditions.**

2.1.1. *Boundary Value Problem.*

For the first model, we consider quasi-1D heat conduction in a conical frustum insulated on the lateral surfaces with heat flux and heat transfer coefficient boundary conditions on the left and right surfaces, respectively. The equations and boundary conditions are given by

$$-k\frac{d}{dx}\left(\pi R_0^2\left(1+\beta\frac{x}{L}\right)^2\frac{du}{dx}\right) = 0 \text{ in } \Omega\ , \tag{1}$$

$$k\frac{du}{dx} = -q_1 \text{ on } \Gamma_1 \ , \tag{2}$$

$$-k\frac{du}{dx} = \eta_2(u - u_\infty) \text{ on } \Gamma_2 \ , \tag{3}$$

where $\Omega = (0, L)$, $\Gamma_1 = \{0\}$, $\Gamma_2 = \{L\}$, k, R_0, L, and η_2 are positive constants, β is a nonnegative constant, and q_1, u_∞ are constants. The exact solution is given by

$$u = u_\infty + \frac{q_1 L}{k}\left(\frac{1+\beta+\frac{k}{\eta_2 L}}{(1+\beta)^2} - \frac{(\frac{x}{L})}{1+\beta(\frac{x}{L})}\right), \tag{4}$$

and the energy functional, $\Pi(w)$, by

$$\begin{aligned}\Pi(w) = \frac{1}{2}\left(\int_0^L k\left(1+\beta\frac{x}{L}\right)^2\left(\frac{dw}{dx}\right)^2 dx + \eta_2(1+\beta)^2 w(L)^2\right) \\ - \left(\eta_2(1+\beta)^2 u_\infty w(L) + q_1 w(0)\right).\end{aligned} \tag{5}$$

Finally, we consider as output

$$s \equiv u(0), \tag{6}$$

the value of the temperature at $x = 0$, the left end of the frustum.

2.1.2. *FEM Formulation.*
In Chapter 1, we considered the Rayleigh-Ritz approximation with basis functions $\{\psi_1 \in X, \psi_1 \in X, ..., \psi_{n^{RR}} \in X\}$ and basis coefficients $\underline{\alpha}^{RR} = (\alpha_1^{RR}\ \alpha_1^{RR}\ ...\ \alpha_{n^{RR}}^{RR}) \in \mathbb{R}^{n^{RR}}$, such that

$$u^{RR}(x) = \sum_{i=1}^{n^{RR}} \alpha_i^{RR}\psi_i(x). \tag{7}$$

We now define a mesh, J_h, with nodes $x^i, 1 \le i \le n_{node}$, and elements $T^m, 1 \le m \le n_{el} = n_{node} - 1$ of uniform length $h^m = h, 1 \le m \le n_{el}$. We define piecewise Rayleigh-Ritz basis functions $\{\psi_i \equiv \varphi_i(x), 1 \le i \le n \equiv n_{node}\}$ where

$$\varphi_i(x^j) = \begin{cases} 1 & j = i \\ 0 & j \ne i \end{cases} \tag{8}$$

For $\mathbb{P}_{p=1}$, $\varphi_i(x)$ is linear on each element and $\varphi_i'(x)$ is constant on each element. Likewise, for $\mathbb{P}_{p=2}$, $\varphi_i(x)$ is quadratic on each element and $\varphi_i'(x)$ is linear on each element. The Rayleigh-Ritz approximation becomes

$$u_h(x^j) = \sum_{i=1}^{n} u_{h_i}\varphi_i(x^j). \tag{9}$$

Because $\varphi_i(x^j)$ is 0 unless $i = j$, and $\varphi_j(x^j) = 1$,

$$u_h(x^j) = u_{h_j}\varphi(x^j) = u_{h_j}. \tag{10}$$

In other words, the j^{th} Rayleigh-Ritz coefficient is equal to the value of $u_h(x)$ at x^j. Substitution of (9) into (5) yields the algebraic form of energy which has first order condition $\underline{A}\underline{u}_h = \underline{F}$, where $\underline{A} \in \mathbb{R}^{n\times n}$ is defined as

$$A_{ij} = \int_0^L k\left(1+\beta\frac{x}{L}\right)^2 \frac{d\varphi_i}{dx}\frac{d\varphi_j}{dx}dx + \eta_2(1+\beta)^2\varphi_i(L)\varphi_j(L), \tag{11}$$

and $\underline{F} \in \mathbb{R}^n$ is defined as

$$F_i = \eta_2(1+\beta)^2 u_\infty \varphi_i(L) + q_1 \varphi_i(0). \tag{12}$$

The output, $u_h(x = 0)$, can be calculated from the basis functions, $\varphi_i(x)$, and Rayleigh-Ritz coefficients, $\underline{u}_h$, that solve the first order condition.

2.1.3. *Verification Techniques.*
Given the exact solution, uniform refinements of the mesh reduce the error estimators in the $H^1(\Omega)$ norm, $L^2(\Omega)$ norm, $L^\infty(\Omega)$ norm, and the output.

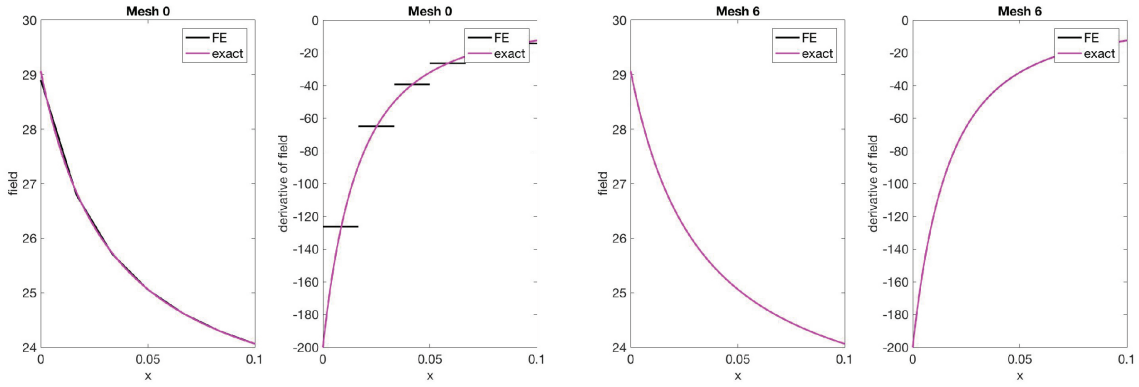

FIGURE 9. For $\mathbb{P}_{P=1}$, the FE approximation, the exact solution and the respective derivatives for the first and final meshes.

For $\mathbb{P}_{P=1}$ we see that the FE solution is piecewise linear and the derivatives are constant, as expected (Figure 9). Beginning with a coarse mesh, a series of 6 uniform refinements are enough to almost exactly approximate the true solution (Figure 9).

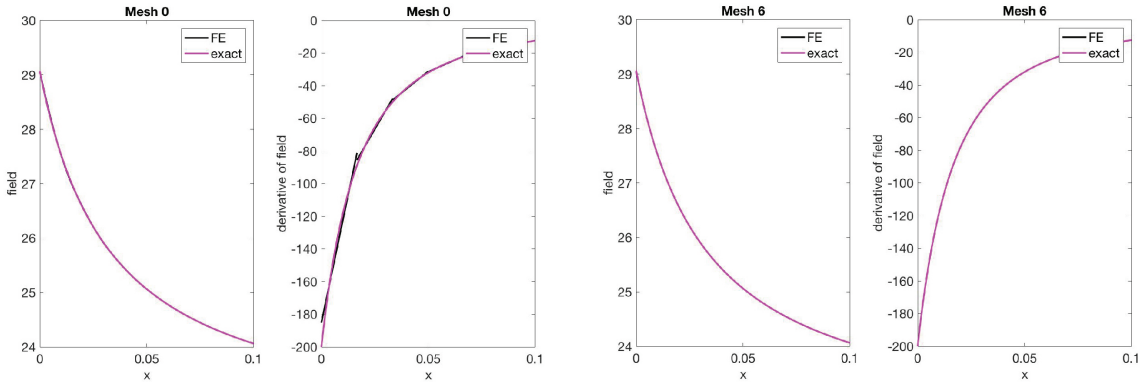

FIGURE 10. For $\mathbb{P}_{P=2}$, the FE approximation, the exact solution and the respective derivatives for the first and final meshes.

Similarly for $\mathbb{P}_{P=2}$ we see that the FE solution is piecewise quadratic, the derivatives are linear, and the finer mesh better approximates the exact solution (Figure 10).

Under the smoothness assumption, as $h \to 0$, convergence of u_h to u and s_h to s is $\mathcal{O}(h^r)$ where

$$\|u - u_h\|_{H^1(\Omega)} \sim C_u h^r,\ r = P \tag{13}$$

$$\|u - u_h\|_{L^2(\Omega)} \sim C_u h^r,\ r = P + 1 \tag{14}$$

$$\|u - u_h\|_{L^\infty(\Omega)} \sim C_u h^r,\ r = P + 0.5 \tag{15}$$

$$|s - s_h| \sim C_u h^r,\ r = 2P \tag{16}$$

Examination of the slope of the $\log_{10}$ error vs $\log_{10}\left(\frac{L}{h}\right)$ plot provides confidence that our implementation is correct, in a particular norm, if the slope is equal to r.

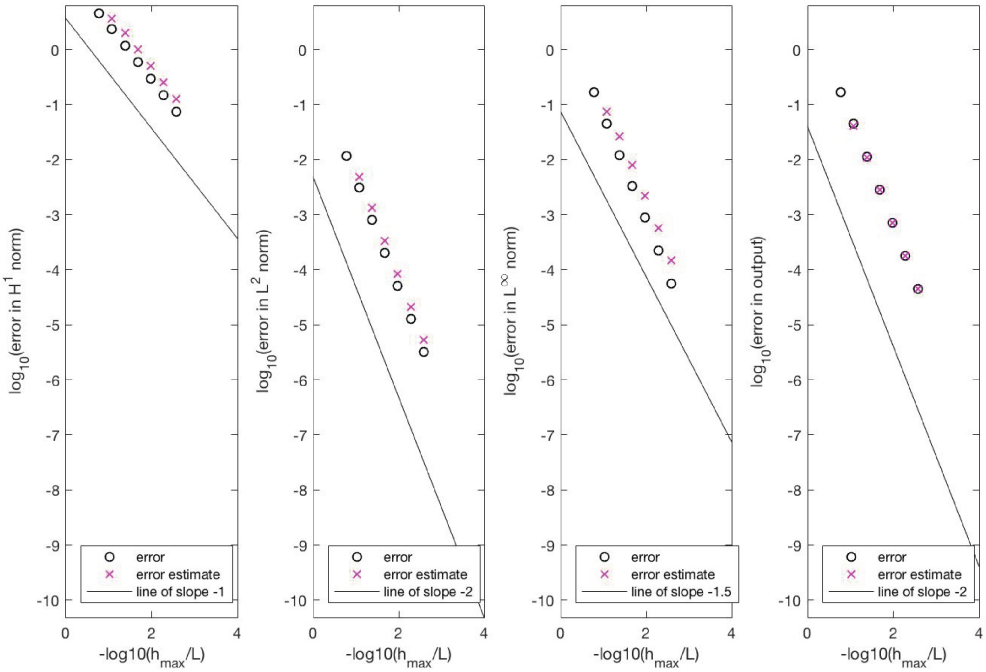

FIGURE 11. Error estimator for $\mathbb{P}_{P=1}$ in $H^1(\Omega)$ norm, $L^2(\Omega)$ norm, $L^\infty(\Omega)$ norm, and the output.

For the $H^1(\Omega)$ norm, we see that u_h is converging to u at the correct rate for $\mathbb{P}_{P=1}$, $C_u h^1$, because the slope is ~ -1 (Figure 11a). Similarly for the $L^2(\Omega)$ norm, $L^\infty(\Omega)$ norm, and output, u_h is converging to u at the correct rates of $C_u h^{1+1}$ and $C_u h^{1+\frac{1}{2}}$, and s_h is converging to s at the correct rate of $C_u h^2$, as shown by the slopes of -2, -1.5, and -2 (Figure 11bcd).

For the $H^1(\Omega)$ norm, we see that u_h is converging to u at the correct rate for $\mathbb{P}_{P=2}$, $C_u h^2$, because the slope is ~ -2 (Figure 12a). Similarly for the $L^2(\Omega)$ norm, $L^\infty(\Omega)$ norm, and output, u_h is converging to u at the correct rates of $C_u h^{2+1}$ and $C_u h^{2+\frac{1}{2}}$, and s_h is converging to s at the correct rate of $C_u h^4$, as shown by the slopes of -3, -2.5, and -4 (Figure 12bcd). While convergence at the correct rate provides confidence that our implementation is correct it does not provide assurance for all model variations.

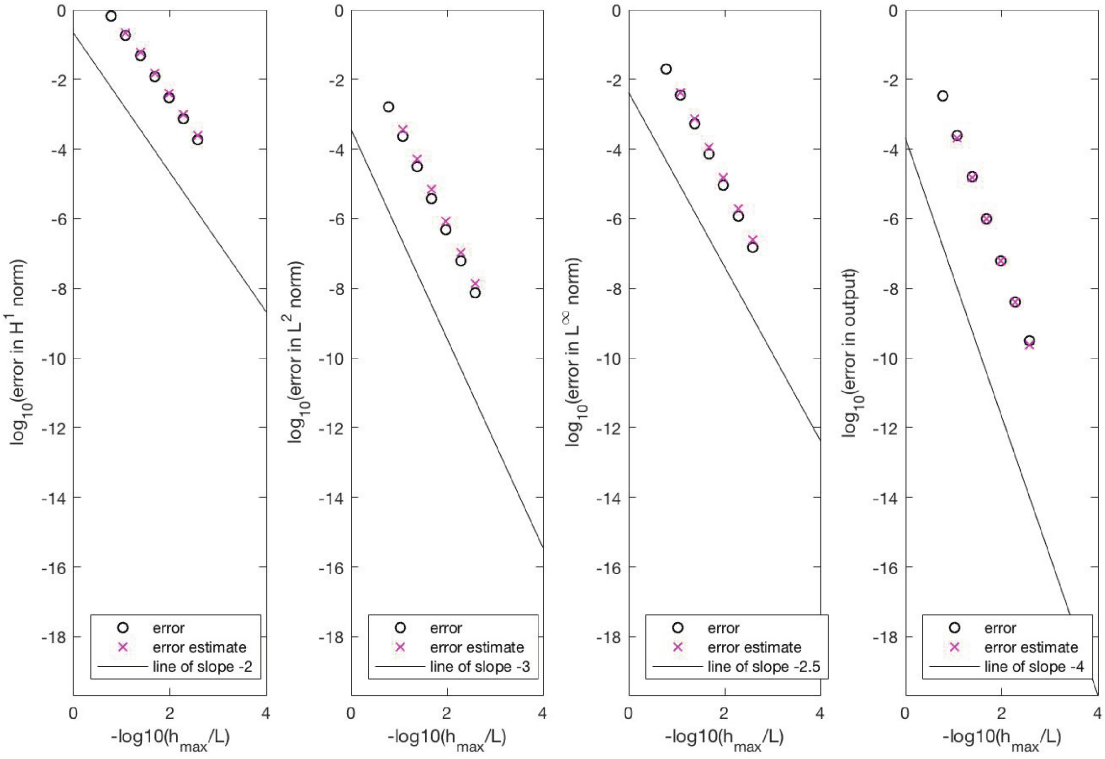

FIGURE 12. Error estimator for $\mathbb{P}_{P=2}$ in $H^1(\Omega)$ norm, $L^2(\Omega)$ norm, $L^\infty(\Omega)$ norm, and the output.

2.2. **Model II: Dirichlet Boundary Conditions.**

2.2.1. *Boundary Value Problem.*

For second model, we consider a right-cylinder thermal fin with temperature and zero-flux boundary conditions on the left and right surfaces, respectively. The equations and boundary conditions are given by

$$-kA_{cs}\frac{d^2u}{dx^2} + \eta_3 P_{cs}(u - u_\infty) = 0 \text{ in } \Omega \ , \tag{17}$$

$$u = u_{\Gamma_1} \text{ on } \Gamma_1 \ , \tag{18}$$

$$-k\frac{du}{dx} = 0 \text{ on } \Gamma_2 \ , \tag{19}$$

where $\Omega = (0, L)$, $\Gamma_1 = \{0\}$, $\Gamma_2 = \{L\}$, k, A_{cs}, P_{cs}, and η_3 are positive constants, and u_{Γ_1} is a constant. The exact solution to this problem is given by

$$u = u_\infty + (u_{\Gamma_1} - u_\infty)\frac{\cosh\left(\sqrt{\mu_0}\left(1 - \frac{x}{L}\right)\right)}{\cosh(\sqrt{\mu_0})}, \tag{20}$$

where $\mu_0 = \frac{\eta_3 P_{cs} L^2}{kA_{cs}}$. The energy functional, $\Pi(w)$, is

$$\Pi(w) = \frac{1}{2}\left(\int_0^L \left[kA_{cs}\left(\frac{dw}{dx}\right)^2 + \eta_3 P_{cs} w^2\right] dx\right) - \int_0^L \eta_3 P_{cs} u_\infty w dx. \tag{21}$$

Finally, we consider as output

$$s \equiv -k\frac{du}{dx}(x = 0), \tag{22}$$

the heat flux into the fin at $x = 0$, the root of the fin.

2.2.2. *FEM Formulation.*
Similar to Model I, substitution of the Rayleigh-Ritz approximation (9) into (21) yields the algebraic form of energy which has first order condition $\underline{A}\underline{u}_h^0 = \underline{F} - u_{\Gamma_1}\underline{b}$. We apply the standard Rayleigh-Ritz procedure, without regard to Dirichlet boundary conditions (Chapter 1.2) to obtain matrices $\underline{\widetilde{A}} \in \mathbb{R}^{n\times n}$

$$\widetilde{A}_{ij} = \int_0^L \left[kA_{cs}\frac{d\varphi_i}{dx}\frac{d\varphi_j}{dx} + \eta_3 P_{cs}\varphi_i(x)\varphi_j(x)\right] dx, \tag{23}$$

and $\underline{\widetilde{F}} \in \mathbb{R}^n$

$$\widetilde{F}_i = \int_0^L \eta_3 P_{cs} u_\infty \varphi_i(x) dx. \tag{24}$$

From $\underline{\widetilde{A}}$ and $\underline{\widetilde{F}}$ we can extract $\underline{A}$, $\underline{b}$, and $\underline{F}$ to solve for $\underline{u}_h^0$. From $\underline{u}_h^0$ and u_{Γ_1} we form $\underline{u}_h$ which is used to construct the solution, $u_h(x)$, and calculate the output $u_h(x = 0)$.

2.2.3. *Verification Techniques.*
Similar to the previous model (Section 2.1.3) uniform refinements of the mesh reduce the error estimators in each norm and in the output.

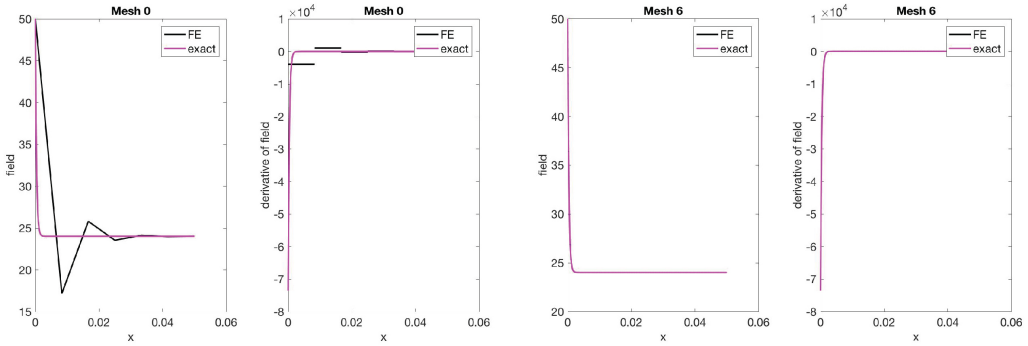

FIGURE 13. For $\mathbb{P}_{P=1}$, the FE approximation, the exact solution, and the respective derivatives for the first and final meshes.

For $\mathbb{P}_{P=1}$ we see that the FE solution is piecewise linear and the derivatives are constant, as expected (Figure 13).

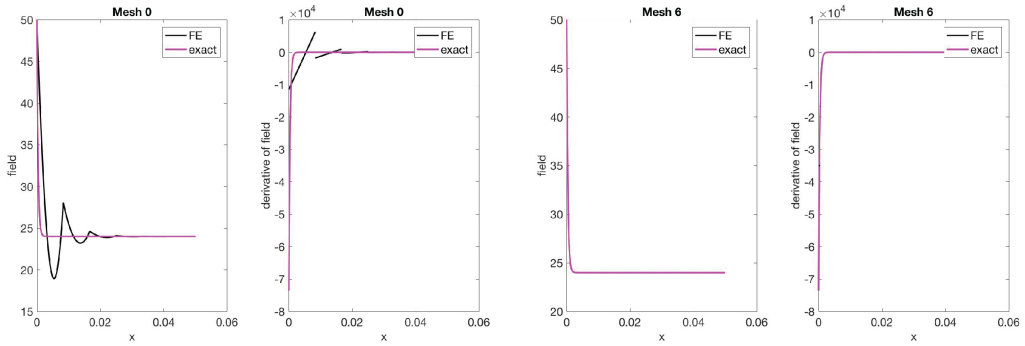

FIGURE 14. For $\mathbb{P}_{P=2}$, the FE approximation, the exact solution and the respective derivatives for the first and final meshes.

For $\mathbb{P}_{P=2}$ we see that the FE solution is piecewise quadratic and the derivatives are linear (Figure 14). Despite a more difficult solution to approximate, a series of 6 uniform refinements are enough to closely approximate the true solution for both $\mathbb{P}_{P=1}$ and $\mathbb{P}_{P=2}$.

As shown in the Section 2.1.3, examination of the slope of the $\log_{10}$ error vs $\log_{10}\left(\frac{L}{h}\right)$ plot provides confidence that our implementation is correct in a particular norm.

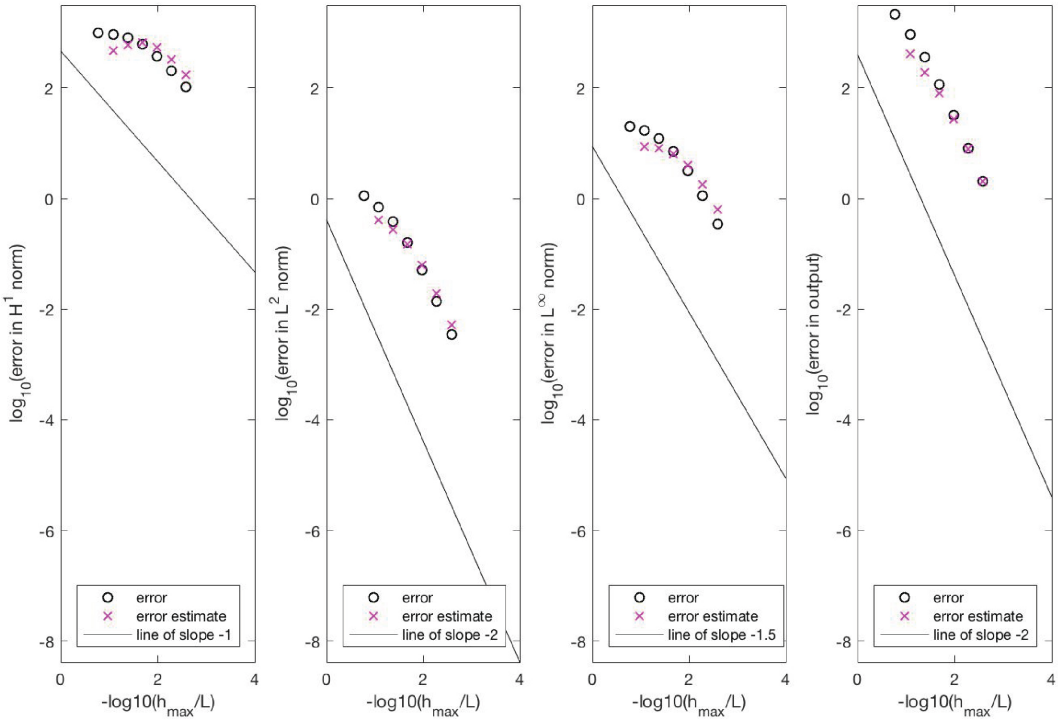

FIGURE 15. Error estimator for $\mathbb{P}_{P=1}$ in $H^1(\Omega)$ norm, $L^2(\Omega)$ norm, $L^\infty(\Omega)$ norm, and the output

In the "linear" regime, for the $H^1(\Omega)$ norm, we see that u_h is converging to u at the correct rate for $\mathbb{P}_{P=1}$, $C_u h^1$, because the slope is ~ -1 (Figure 15a). Similarly for the $L^2(\Omega)$ norm, $L^\infty(\Omega)$ norm, and output, u_h is converging to u at the correct rates of $C_u h^{1+1}$ and $C_u h^{1+\frac{1}{2}}$, and s_h is converging to s at the correct rate of $C_u h^2$, as evidenced by the slopes of -2, -1.5, and -2 (Figure 15bcd). We can only trust the error estimators in the region where they are beginning to converge, discounting initial increases. Specifically, the error estimator in the $H^1(\Omega)$ norm increases as we refine on the first few meshes because the refinements are actually amplifying errors in the approximation. However with further refinements, we see u_h start to converge to u and the error estimator in that norm decrease at the rate we would expect.

Again, we must be careful to consider only the asymptotic convergent state. For the $H^1(\Omega)$ norm, we see that u_h is converging to u at the correct rate for $\mathbb{P}_{P=2}$, $C_u h^2$, because the slope is ~ -2 (Figure 16a). Similarly for the $L^2(\Omega)$ norm, $L^\infty(\Omega)$ norm, and output, u_h is converging to u at the correct rates of $C_u h^{2+1}$ and $C_u h^{2+\frac{1}{2}}$, and s_h is converging to s at the correct rate of $C_u h^4$, as shown by the slopes of -3, -2.5, and -4 (Figure 16bcd).

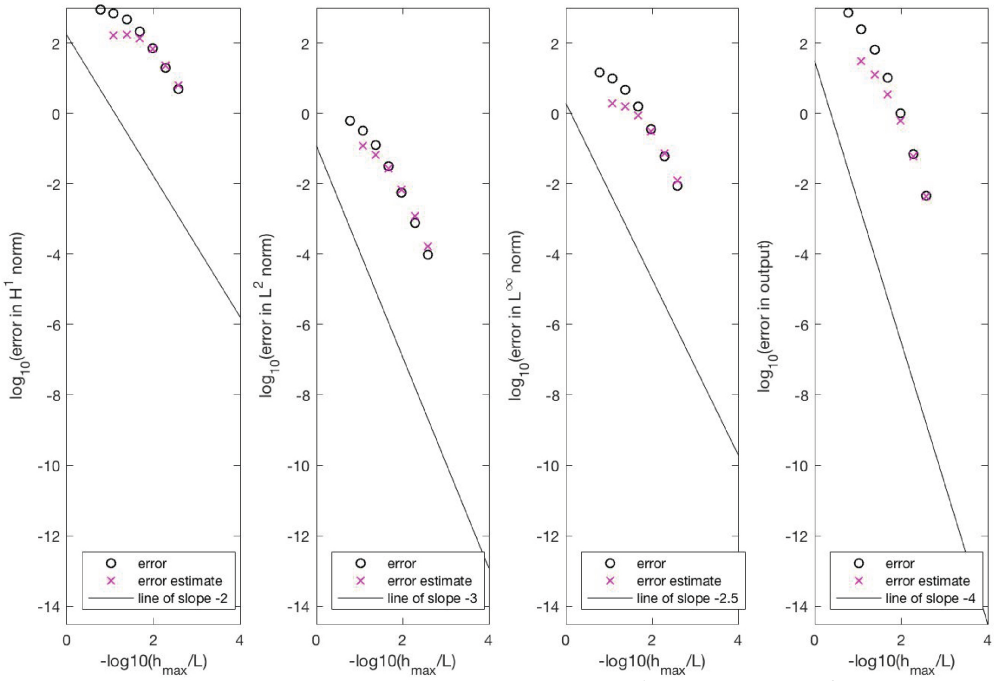

FIGURE 16. Error estimator for $\mathbb{P}_{P=2}$ in $H^1(\Omega)$ norm, $L^2(\Omega)$ norm, $L^\infty(\Omega)$ norm, and the output.

Previously, we considered the FE solution to this model, provided knowledge of the exact solution, and on a sequence of 7 meshes. To assess the accuracy of the FE solution in a realistic context, we will now assume the exact solution is not available and increase the number of refinements on the mesh from 6 to 8.

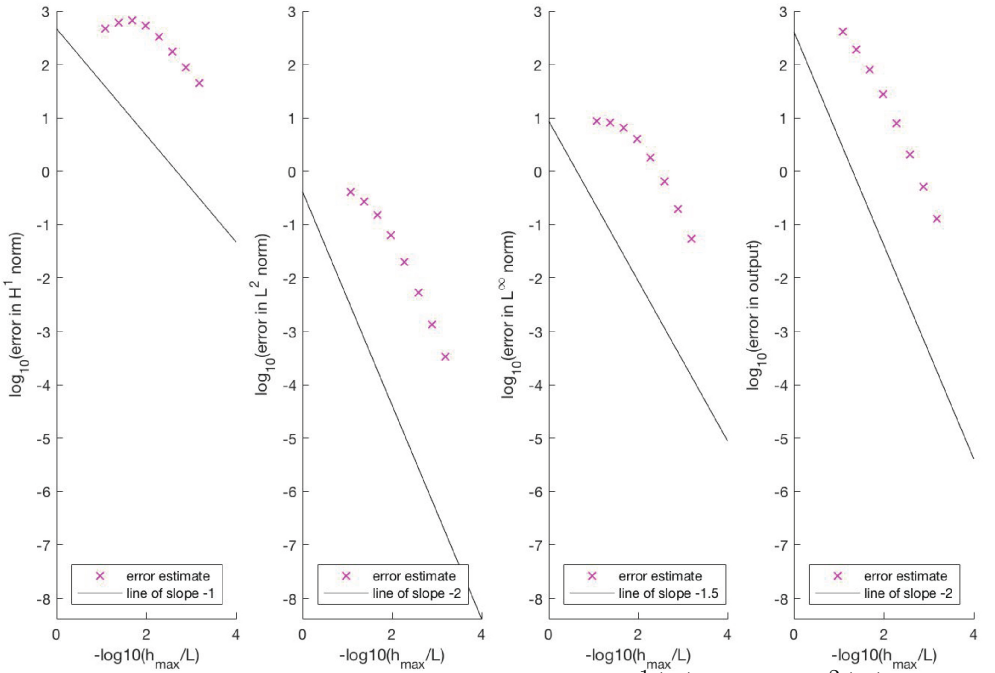

FIGURE 17. Error estimator for $\mathbb{P}_{P=1}$ in $H^1(\Omega)$ norm, $L^2(\Omega)$ norm, $L^\infty(\Omega)$ norm, and the output.

For $\mathbb{P}_{P=1}$, the coarsest mesh such that $\|u - u_h\|_{L^\infty(\Omega)}$ over all $x \in \Omega$ is less than 1.00, is mesh 7 (Figure 17c). For this mesh, the error in the $L^\infty(\Omega)$ norm is $10^{-0.1967} = 0.9557$ (Figure 17c). For mesh 6, the error in the $L^\infty(\Omega)$ norm is $10^{-0.2521} = 1.787$ (Figure 17c). A very conservative estimate of the upper bound for $|u - u_h\|_{L^\infty(\Omega)}$ on mesh 7 could be 1.7 because we know in the asymptotic convergent state a refinement from mesh 6 to 7 will decrease the error estimator. For mesh 5, the error in the output is $10^{1.443} = 27.73$ and for mesh 4, the error in the output is $10^{1.908} = 80.91$ (Figure 17d). Likewise, a very conservative upper bound for $|s - s_h|$ on mesh 5 could be 80.9 for the same reason as above.

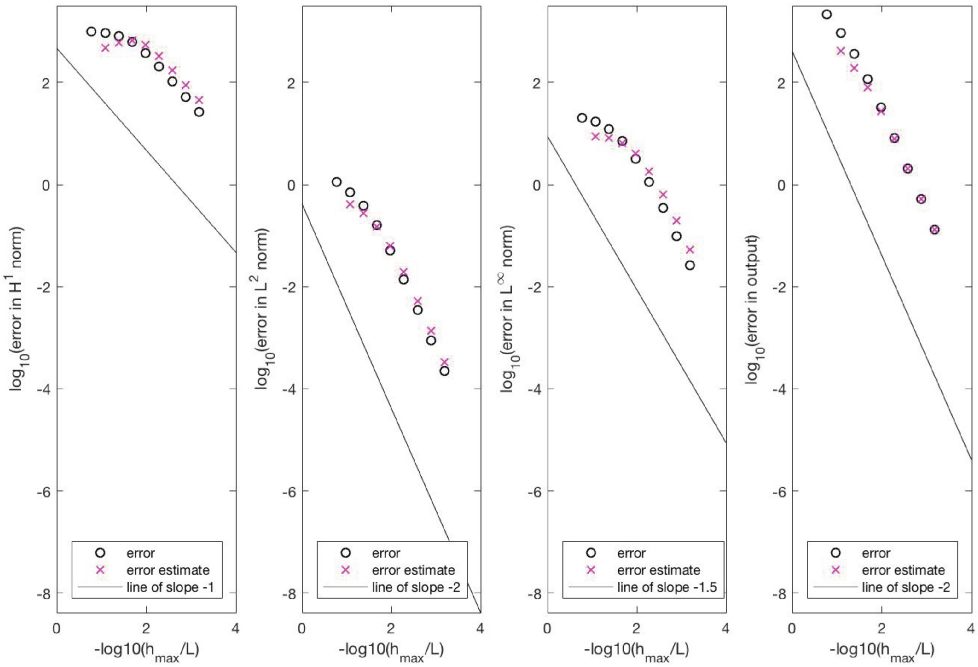

FIGURE 18. Error estimator for $\mathbb{P}_{P=1}$ in $H^1(\Omega)$ norm, $L^2(\Omega)$ norm, $L^\infty(\Omega)$ norm, and the output.

Upon examination of the exact error in the $L^\infty(\Omega)$ norm and in the output, both fall below the chosen upper bounds (Figure 18cd). Although choosing a conservative upper bound on the error estimator for a particular mesh could result in unnecessary added computation there is less risk of choosing a mesh that is not sufficient to obtain the accuracy needed.

2.3. **Model III: Robin/Robin Boundary Conditions.**

2.3.1. *Boundary Value Problem.*

For the third model, we consider a right-cylinder with heat transfer coefficient boundary conditions on the left and right surfaces. The equations and boundary conditions are given by

$$-kA_{cs}\frac{d}{dx}\left(\frac{du}{dx}\right) = 0 \text{ in } \Omega \ , \tag{25}$$

$$k\frac{du}{dx} = \eta_1(u - u_{out}) \text{ on } \Gamma_1 \ , \tag{26}$$

$$-k\frac{du}{dx} = \eta_2(u - u_{in}) \text{ on } \Gamma_2 \ , \tag{27}$$

where $\Omega = (0, L)$, $\Gamma_1 = \{0\}$, $\Gamma_2 = \{L\}$, k, A_{cs}, η_1 and η_2 are positive constants, and u_{in}, u_{out} are constants. The exact solution to this problem is given by

$$u = \left[\frac{u_{in} - u_{out}}{\frac{kA_{cs}}{\eta_1 L} + \frac{kA_{cs}}{\eta_2 L} + 1}\right]\frac{x}{L} + \left[\frac{kA_{cs}}{\eta_1 L}\left(\frac{u_{in} - u_{out}}{\frac{kA_{cs}}{\eta_1 L} + \frac{kA_{cs}}{\eta_2 L} + 1}\right) + u_{out}\right] \tag{28}$$

and the energy functional, $\Pi(w)$, by

$$\begin{aligned}\Pi(w) = &\frac{1}{2}\left(\int_0^L \left[kA_{cs}\left(\frac{dw}{dx}\right)^2\right]dx\right) \\ &+ \frac{1}{2}\left(\eta_1 A_{cs} w(0)^2 + \eta_2 A_{cs} w(L)^2\right) - \eta_1 A_{cs} u_{out} w(0) - \eta_2 A_{cs} u_{in} w(L).\end{aligned} \tag{29}$$

Finally, we consider as output

$$s \equiv u(0), \tag{30}$$

the value of the temperature at $x = 0$, the left end of the cylinder.

2.3.2. *FEM Formulation.*
Substitution of (9) into (25) yields the algebraic form of energy which has first order condition $\underline{A}\underline{u}_h = \underline{F}$, where $\underline{A} \in \mathbb{R}^{n\times n}$ is defined as

$$A_{ij} = \int_0^L kA_{cs}\frac{d\varphi_i}{dx}\frac{d\varphi_j}{dx}dx + \eta_1 A_{cs}\varphi_i(0)\varphi_j(0) + \eta_2 A_{cs}\varphi_i(L)\varphi_j(L) \tag{31}$$

and $\underline{F} \in \mathbb{R}^n$ is defined as

$$F_i = \eta_1 u_{out} A_{cs}\varphi_i(0) + \eta_2 u_{in} A_{cs}\varphi_i(L). \tag{32}$$

The output, $u_h(x = 0)$, can be calculated from the basis functions, $\varphi_i(x)$, and Rayleigh-Ritz coefficients, $\underline{u}_h$, that solve the first order condition.

2.3.3. *Verification Techniques.*
Again, we perform a series of uniform refinements on the mesh to reduce the error estimators in each norm and in the output

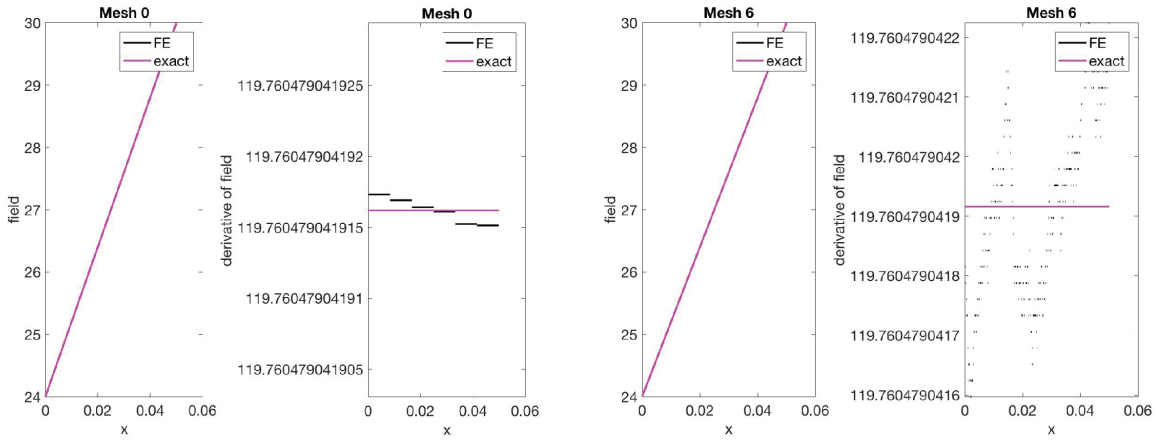

FIGURE 19. For $\mathbb{P}_{P=1}$, the FE approximation, the exact solution, and the respective derivatives for the first and final meshes.

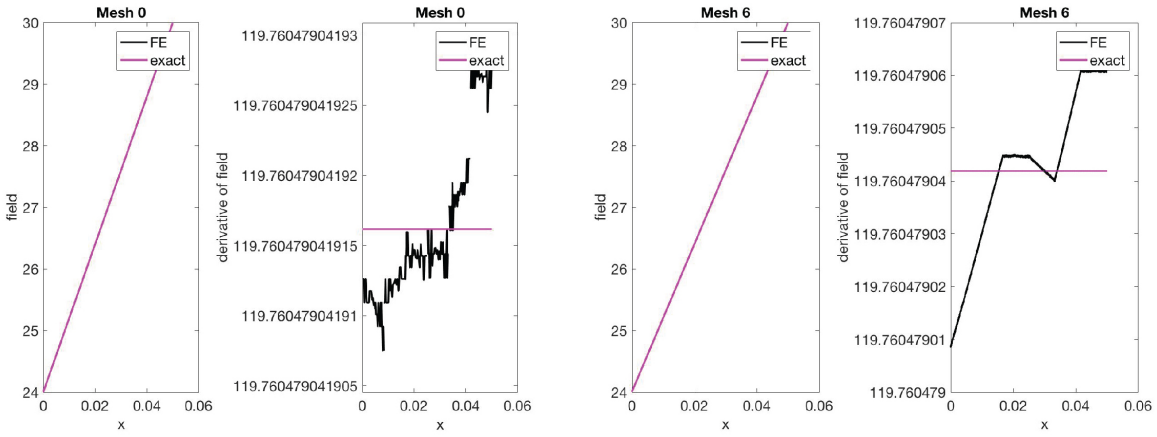

FIGURE 20. For $\mathbb{P}_{P=2}$, the FE approximation, the exact solution and the respective derivatives for the first and final meshes.

Because our exact solution (28) is linear, further refinements to the mesh for both $\mathbb{P}_{P=1}$ and $\mathbb{P}_{P=2}$ don't provide significantly better approximations, unlike Model I and Model II.

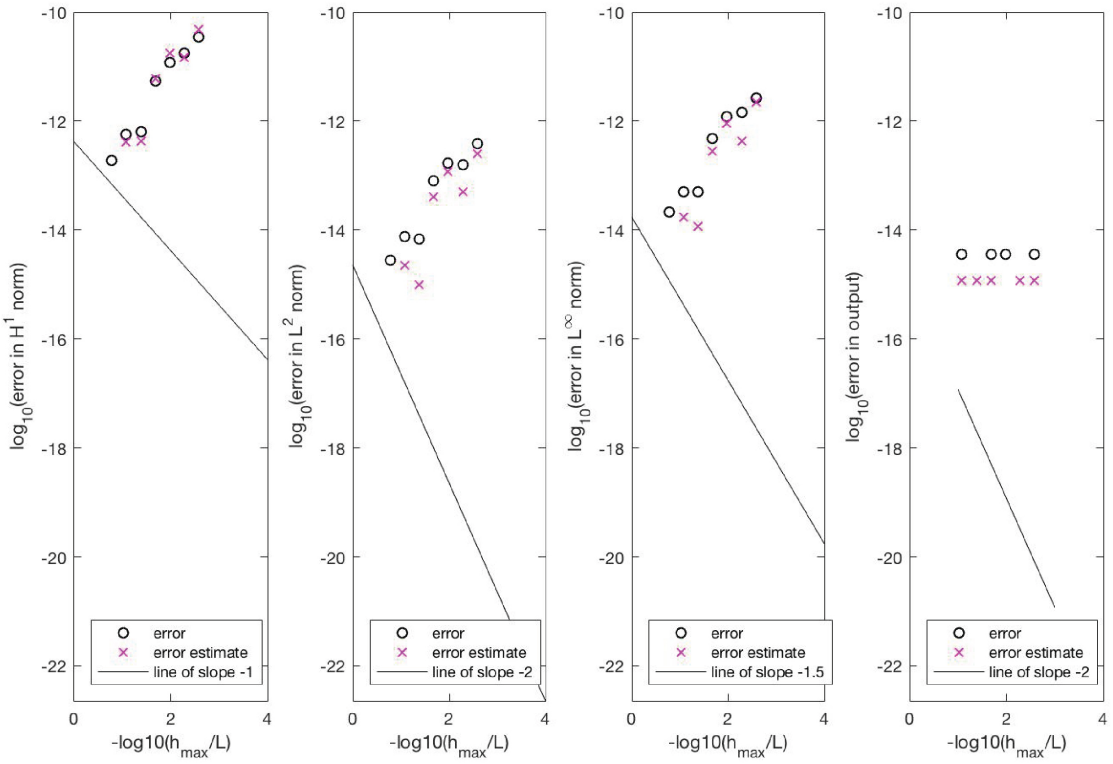

FIGURE 21. Error estimator for $\mathbb{P}_{P=1}$ in $H^1(\Omega)$ norm, $L^2(\Omega)$ norm, $L^\infty(\Omega)$ norm, and the output.

For $\mathbb{P}_{P=1}$, the error estimator appears to be increasing, as we refine the mesh. However, if we examine the y-axis, the $\log_{10}$ error measured in all norms and in the output ranges from about -10 to -16 which is very small. Therefore, we can assume this

error is due to finite precision and are provided with confidence that our implementation is correct.

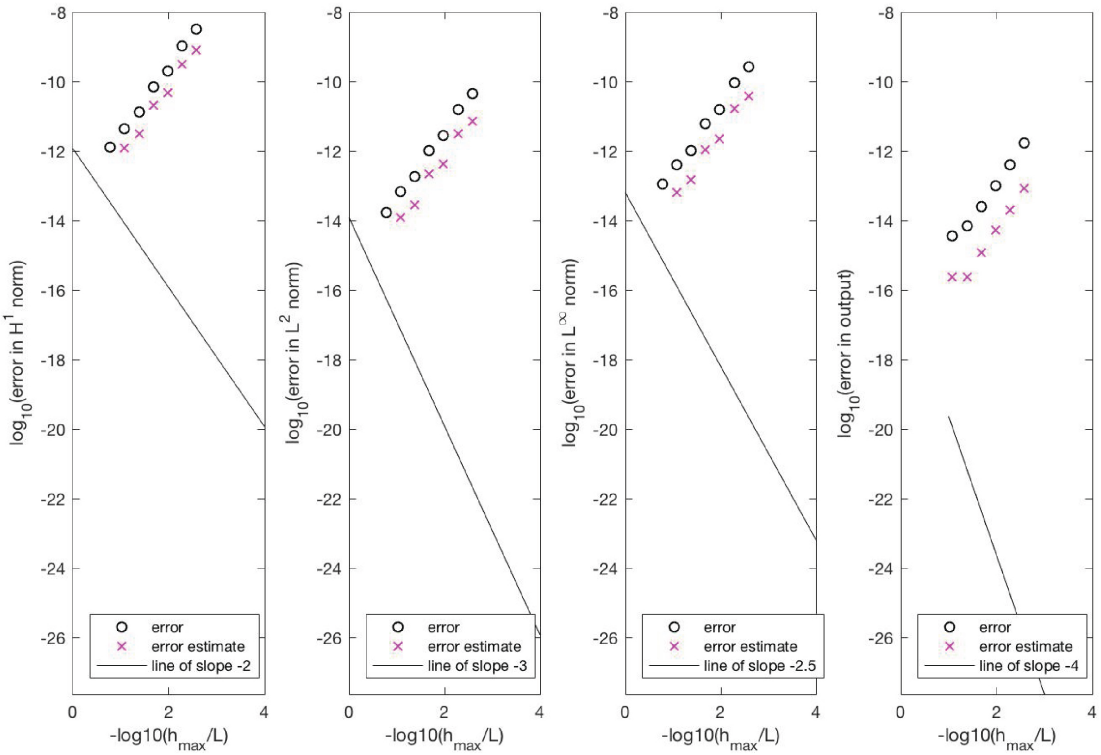

FIGURE 22. Error estimator for $\mathbb{P}_{P=2}$ in $H^1(\Omega)$ norm, $L^2(\Omega)$ norm, $L^\infty(\Omega)$ norm, and the output.

Similarly, for $\mathbb{P}_{P=2}$ the apparent divergence in the error estimator, as measured in each norm and the output, is a result of finite precision.

2.4. **Verification, Convergence, and Error Estimators.**

Although convergence of u_h to u at the correct rate provided us with confidence that the implementation was correct it does not provide assurance for all possible instantiations of $\mu(x)$. The third model (Section 2.3) provides greater implementation confidence than the first model (Section 2.1). For the first model, the $\mu(x)$, $f_\Omega(x)$, and γ_1 terms are all zero. Whereas the third model, only $\mu(x)$ and $f_\Omega(x)$ terms are zero. Therefore, had we made an implementation error when we imposed N/R-N/R boundary conditions, particularly when adding the γ_1 term, the first model would not have been affected while the third would.

Using the method of manufactured solutions we can define another model that could provide additional confidence that our implementation is correct. We consider the general form for our energy functional, $\Pi(w)$

$$\begin{aligned}\Pi(w) = \frac{1}{2}\left(\int_0^L \left[\kappa(x)\left(\frac{dw}{dx}\right)^2 + \mu(x)w^2\right]dx\right) + \frac{1}{2}\left(\gamma_1 w^2(0) + \gamma_2 w^2(L)\right) \\ - \int_0^L f_\Omega(x) w dx - w(0) f_{\Gamma_1} - w(L) f_{\Gamma_2}.\end{aligned} \tag{33}$$

An ideal model to test implementation would account for all terms. In other words, $\kappa(x)$, $\mu(x)$, $f_\Omega(x)$, f_{Γ_1}, f_{Γ_2}, γ_1, and γ_2 would all be nonzero. Additionally, as we saw in Model II, $\mu(x)$ was a constant which does not properly test the case where μ is a function of x. Therefore, we must also construct the model such that functions are not given constant values.

Despite accounting for all terms, convergence of u_h to u at the correct rate does not prove implementation is correct. For example, consider a model for which the exact solution is not known. We run the FE code and observe that for sufficiently small h the extrapolation error estimators converge at the anticipated rates in all norms. This is not enough to conclude that u_h is converging to the exact solution u of the model. As a counterexample, suppose we forgot to call `library_of_models`. The function `FE1d_uniform_refinement` might then use a `probdef` from an earlier case in `run_uniform_refinement`. The error estimators in all norms would still converge at the right rates but u_h would not be converging to the correct exact solution, u, of the model.

3. The FD-FE Method for the 1D Heat Equation

In this chapter, we examine the FE method as applied to time-dependent problems, specifically the heat equation.

3.1. N/R-N/R boundary conditions.

We consider the general form for a time-dependent, boundary value problem. The equations and boundary conditions are given by

$$-\frac{\partial}{\partial x}\left(\kappa(x)\frac{\partial u}{\partial x}\right)+\mu(x)u=f_\Omega(x)-\rho(x)\dot{u}\quad\text{in }\Omega,\ 0<t\le t_f, \tag{1}$$

$$\kappa\frac{\partial u}{\partial x}=\gamma_1 u-f_{\Gamma_1}\quad\text{on }\Gamma_1,\ 0<t\le t_f, \tag{2}$$

$$-\kappa\frac{\partial u}{\partial x}=\gamma_2 u-f_{\Gamma_2}\quad\text{on }\Gamma_2,\ 0<t\le t_f, \tag{3}$$

$$u=u_{ic}(x)\quad\text{in }\Omega, t=0 \tag{4}$$

where $\Omega=(0,L)$, $\Gamma_1=\{0\}$, $\Gamma_2=\{L\}$. We assume $\kappa(x)>0$, $\rho(x)>0$, and $\mu(x)\ge 0$, $\forall x\in\Omega$ and $\gamma_1\ge 0,\gamma_2\ge 0$. The energy functional $\Pi(w)$ now takes the form

$$\begin{aligned}\Pi(w)=\frac{1}{2}\left(\int_0^L\left[\kappa(x)^2\left(\frac{dw}{dx}\right)^2+\mu(x)w^2\right]dx+\gamma_1 w^2(0)+\gamma_2 w^2(L)\right)\\-\left(\int_0^L f_\Omega^+(x)w dx+f_{\Gamma_1}w(0)+f_{\Gamma_2}w(L)\right),\end{aligned} \tag{5}$$

where $f_\Omega^+(x)=f_\Omega-\rho(x)\dot{u}$.

3.1.1. *Finite Element Forumlation.*
The time derivative of the solution can be approximated by

$$u(x,t) \approx u_h(x,t) = \sum_{j=1}^{n} u_{h_j}(t)\varphi_j(x) \tag{6}$$

$$\dot{u}(x,t) \approx \dot{u}_h(x,t) = \sum_{j=1}^{n} \dot{u}_{h_j}(t)\varphi_j(x) \tag{7}$$

Substitution of (6) into (5) yields the algebraic form of energy which has first order condition $\underline{M}^{inertia}\dot{\underline{u}}_h + \underline{A}\underline{u}_h = \underline{F}$ for $0 < t \leq t_f$ and $\underline{u}_h = \underline{(I_h u_{ic})}$ for $t = 0$ where $\underline{M}^{inertia}$ is defined as

$$M^{inertia} = \int_0^L \rho(x)\varphi_i\varphi_j dx \qquad 1 \leq i,j \leq n, \tag{8}$$

$\underline{A}$ is defined as

$$\begin{aligned} A_{ij} = \int_0^L \left[\kappa(x)^2 \frac{d\varphi_i}{dx}\frac{d\varphi_j}{dx} + \mu(x)\varphi_i\varphi_j\right] dx \\ + \gamma_1\varphi_i(0)\varphi_j(0) + \gamma_2\varphi_i(L)\varphi_j(L) \qquad 1 \leq i,j \leq n, \end{aligned} \tag{9}$$

and $\underline{F}$ is defined as

$$F_i = \int_0^L f_\Omega\varphi_i dx + f_{\Gamma_1}\varphi_i(0) + f_{\Gamma_2}\varphi_i(L) \qquad 1 \leq i \leq n. \tag{10}$$

3.1.2. *Finite Difference Temporal Discretization.*
For this system of n ODEs in time, the first order temporal discretization of the heat equation is given by

$$\underline{M}^{inertia}\frac{\underline{u}^k_{h,\Delta t} - \underline{u}^{k-1}_{h,\Delta t}}{\Delta t} + \underline{A}(\theta\underline{u}^k_{h,\Delta t} + (1-\theta)\underline{u}^{k-1}_{h,\Delta t}) = \underline{F} \qquad 2 \leq k \leq n_{steps}, \tag{11}$$

$$\underline{u}^k_{h,\Delta t} = \underline{(I_h u_{ic})} \qquad k = 1. \tag{12}$$

where the FE(h)-FD(Δt) solution at time step k

$$\underline{u}^k_{h,\Delta t}(x) \approx u(x,t^k), \qquad 1 \leq k \leq n_{steps}, \tag{13}$$

and the chosen finite difference method is given by

$$\theta = \begin{cases} 0 & : \text{Euler Forward} \\ \frac{1}{2} & : \text{Crank-Nicolson} \\ 1 & : \text{Euler Backward} \end{cases} \tag{14}$$

3.2. **Verification, Convergence, and Error Estimators.**

For time-dependent problems, there is convergence in both the temporal and the spatial domains. Under the smoothness assumption, as $h \to 0$ and $\Delta t \to 0$

$$\left\| u(\cdot, t_f) - u_{h,\Delta t}^{n_{tsteps}} \right\|_Q \sim C_{u,Q}^1 \left(\frac{\Delta t}{\Delta t_0} \right)^q + C_{u,Q}^2 \left(\frac{h}{h_0} \right)^r, \tag{15}$$

where the temporal convergence rates, $q(\theta)$, are given by

$$q = \begin{cases} 1 & \theta = 1 \text{ (Euler Backward)} \\ 2 & \theta = 0.5 \text{ (Crank-Nicolson)} \end{cases} \tag{16}$$

and the spatial convergence rates, $r(P, Q)$, are given by

$$r = \begin{cases} P & Q \equiv H^1(\Omega) \\ P+1 & Q \equiv L^2(\Omega) \\ P+1/2 & Q \equiv L^\infty(\Omega) \\ 2P & Q \equiv \text{output}, \ |s(t_f) - s_{h,\Delta t}^{n_{tsteps}}| \end{cases} \tag{17}$$

For a series of uniform refinements, ℓ, we can express the convergence rate as

$$\left\| u(\cdot, t_f) - u_{h,\Delta t}^{n_{tsteps}} \right\|_Q^\ell \sim 2^{-r\ell} \left(C_{u,Q}^1 \left(\frac{2^r}{\sigma^q} \right)^\ell + C_{u,Q}^2 \right), \tag{18}$$

for $l \to \infty$. In the $L^2(\Omega)$ norm, (18) can be rewritten as

$$\left\| u(\cdot, t_f) - u_{h,\Delta t}^{n_{tsteps}} \right\|_Q^\ell \sim C_{u,Q} 2^{-r\ell} \text{ for } C_{u,Q} = C_{u,Q}^1 + C_{u,Q}^2. \tag{19}$$

In principle, reference values Δt_0 and h_0 should be chosen such that $C_{u,Q}^1 \approx C_{u,Q}^2$.

3.3. **Model `semiinf_plus`.**

Given the exact solution, uniform refinements of the mesh reduce the error estimators in the $H^1(\Omega)$ norm, $L^2(\Omega)$ norm, $L^\infty(\Omega)$ norm, and the output.

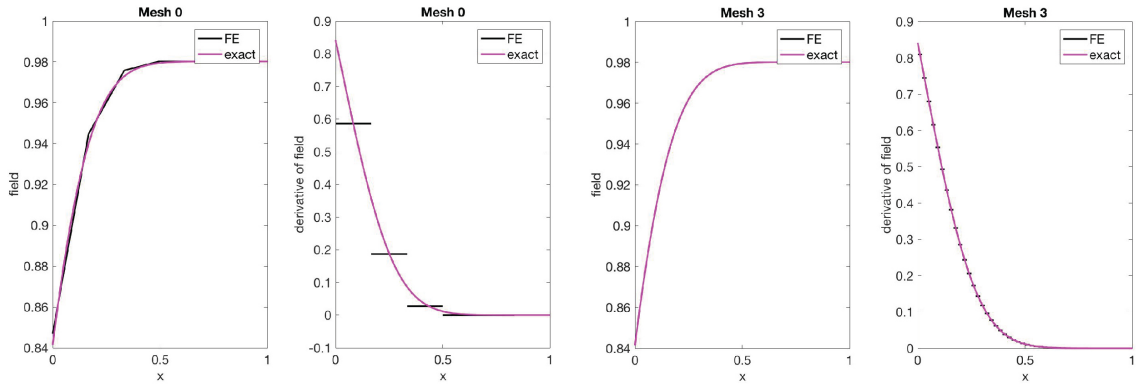

FIGURE 23. For $\mathbb{P}_{P=1}$ and $\theta = 1$ (Euler Backward), the FE-FD approximation, the exact solution, and the respective derivatives for the first and final meshes.

For $\mathbb{P}_{P=1}$ and $\theta = 1$ we see that the FE-FD solution is piecewise linear and the derivatives are constant, as expected (Figure 23). Beginning with a coarse mesh, a series of 3 uniform refinements are enough to closely approximate the exact solution.

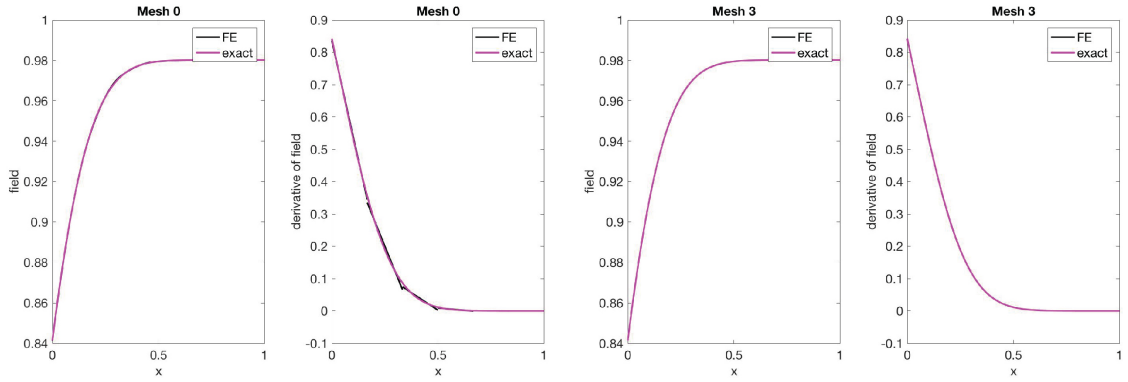

FIGURE 24. For $\mathbb{P}_{P=2}$ and $\theta = 0.5$ (Crank-Nicolson), the FE approximation, the exact solution and the respective derivatives for the first and final meshes.

For $\mathbb{P}_{P=2}$ and $\theta = 0.5$ the FE-FD method performs better because the exact solution can be more closely approximated with quadratic functions than with linear functions. As expected, the FE solution is piecewise quadratic and the derivatives are linear (Figure 24). Similarly, beginning with a coarse mesh, a series of 3 uniform refinements are enough to almost exactly approximate the true solution (Figure 24).

As shown in Section 3.2, examination of the slope of the $\log_{10}$ error vs $\log_{10}(\frac{L}{h_{max}})$ plot provides confidence that our implementation is correct in a particular norm.

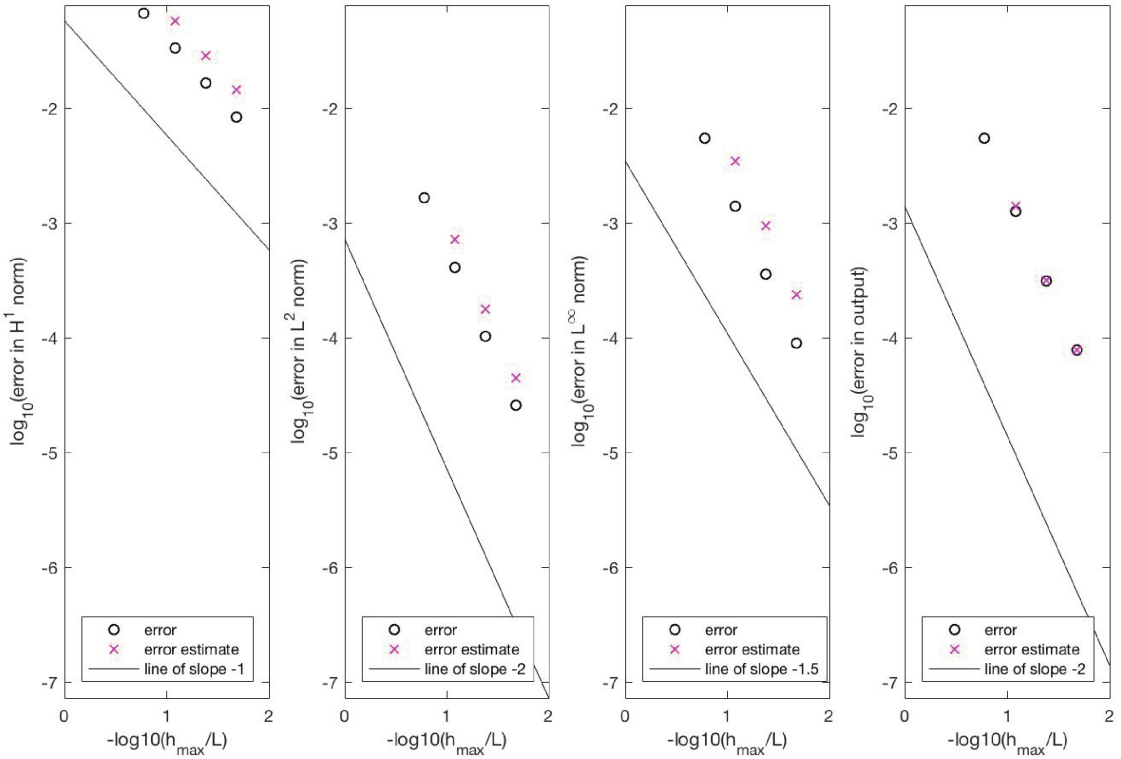

FIGURE 25. Error estimator for $\mathbb{P}_{P=1}$ and $\theta = 1$ in $H^1(\Omega)$ norm, $L^2(\Omega)$ norm, $L^\infty(\Omega)$ norm, and the output.

For the $L^2(\Omega)$ norm we see that $\underline{u}^k_{h,\Delta t}(x)$ is converging to $u(x,t^k)$ at the correct rate for $\mathbb{P}_{P=1}$ and $\theta = 1$, $C_{u,Q}2^{-2l}$, because the slope is ~ -2 (Figure 25b).

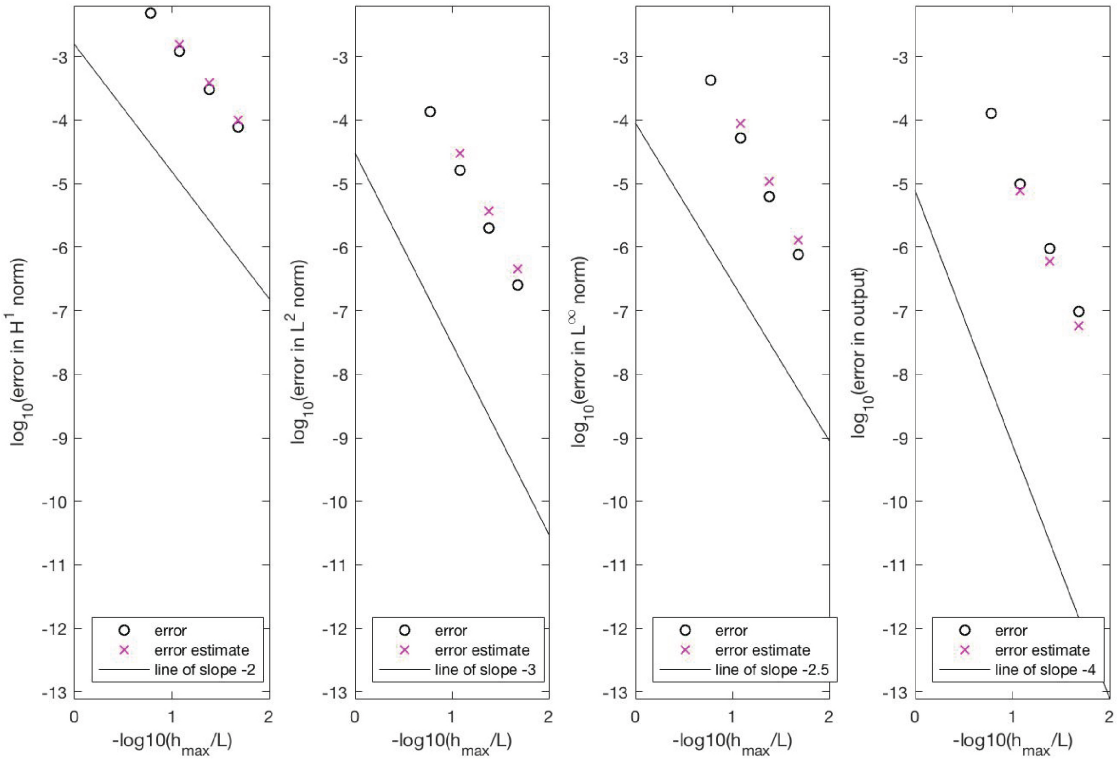

FIGURE 26. Error estimator for $\mathbb{P}_{P=2}$ and $\theta = 0.5$ in $H^1(\Omega)$ norm, $L^2(\Omega)$ norm, $L^\infty(\Omega)$ norm, and the output.

Similarly, for the $L^2(\Omega)$ norm we see that $\underline{u}^k_{h,\Delta t}(x)$ is converging to $u(x,t^k)$ at the correct rate for $\mathbb{P}_{P=2}$ and $\theta = 0.5$, $C_{u,Q}2^{-3l}$, because the slope is ~ -3 (Figure 26b).

3.4. **Model** `burger`.

3.4.1. *Verification of Implementation.*

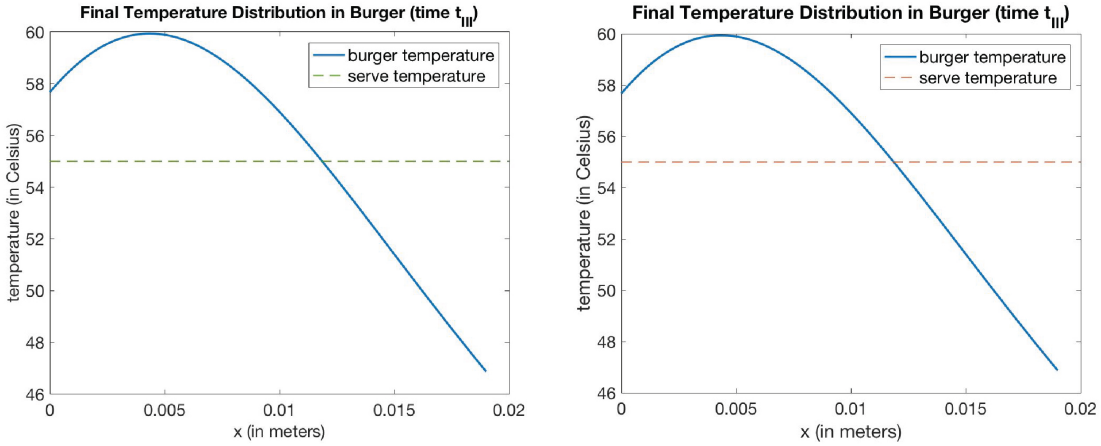

FIGURE 27. Final temperature distribution results for our implementation (a) and a third party implementation (b).

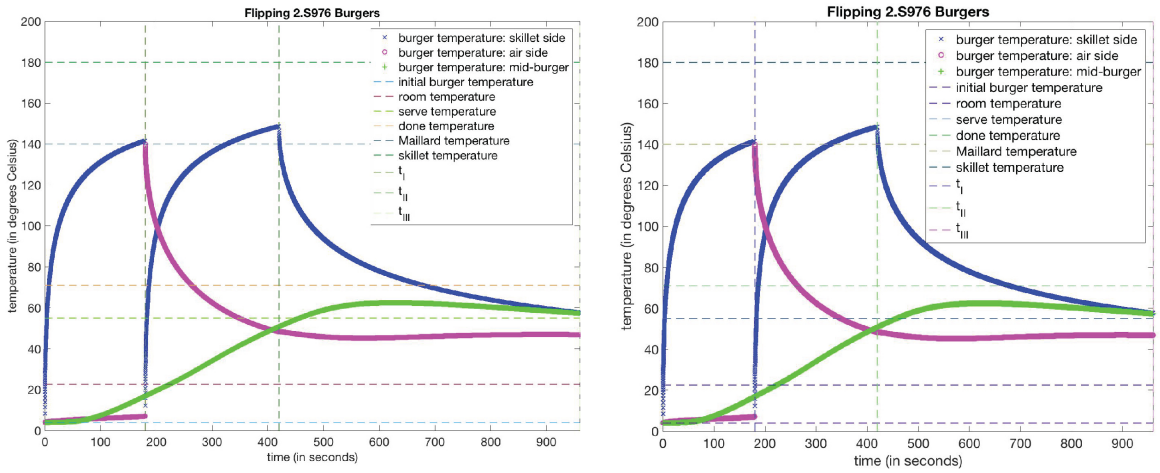

FIGURE 28. Burger temperatures as a function of time at the skillet side, air side, and in the middle for our implementation (a) and a third party implementation (b).

Because the reference code and our code share the same underlying numerical approximation, at tight error tolerances, direct comparison can provide confidence that our implementation is correct. We see that the final temperature distribution in the burger as a function of distance (Figure 27a), and the temperatures at various points in the burger as a function of time (Figure 28a) resemble exactly those generated by the reference model (Figures 27b, 28b).

3.4.2. *Verification of Numerical Specifications.*
To verify our numerical specifications we will consider an error tolerance of $0.001°C$ in the output (the burger temperature T^I at the skillet side at time t^I, just before the flip). For $\mathbb{P}_{P=1}$ and $\theta = 1$, the coarsest FE mesh for which the error in the output is less than $0.001°C$ is mesh 6 (Figure 29d). However, for $\mathbb{P}_{P=2}$ and $\theta = 0.5$, the coarsest FE mesh for which the error in the output is less than $0.001°C$ is mesh 2 (Figure 30d). We see that the higher order method, $\mathbb{P}_{P=2}$, has a large advantage over the lower order one, $\mathbb{P}_{P=1}$, in that far less refinements are needed to achieve our desired error tolerance.

For a series of ℓ uniform refinements, the operation count is $\mathcal{O}((\frac{L}{h_0/2^\ell})^2)$. For our purposes we will consider how the $2^{2\ell}$ term scales. For $\mathbb{P}_{P=1}$ and $\theta = 1$, five refinements cause the operation count to be $\mathcal{O}(2^{10}(\frac{L}{h_0})^2)$. For $\mathbb{P}_{P=2}$ and $\theta = 0.5$, the operation count to solve a pentadiagonal system is twice that of a tri-diagonal system. However, only one refinement is needed so the operation is $\mathcal{O}(2^3(\frac{L}{h_0})^2)$. Therefore, the second approach, $\mathbb{P}_{P=2}$ and $\theta = 0.5$, is much more efficient computationally.

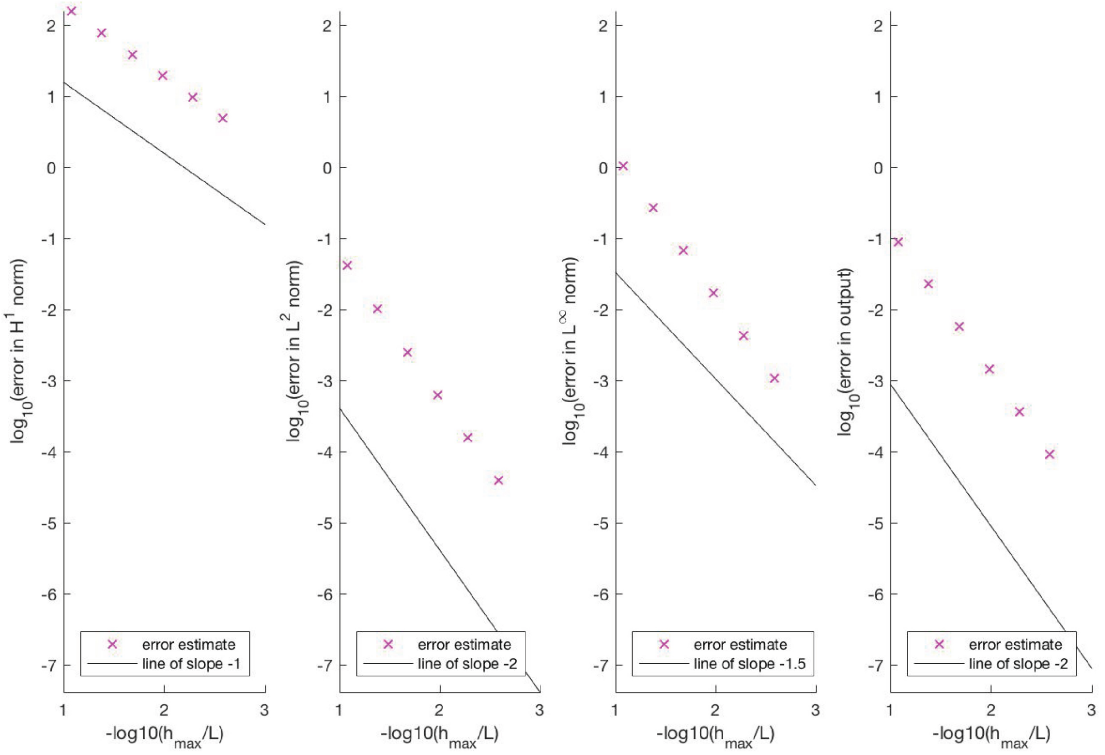

FIGURE 29. Error estimator for $\mathbb{P}_{P=1}$ and $\theta = 1$ in $H^1(\Omega)$ norm, $L^2(\Omega)$ norm, $L^\infty(\Omega)$ norm, and the output.

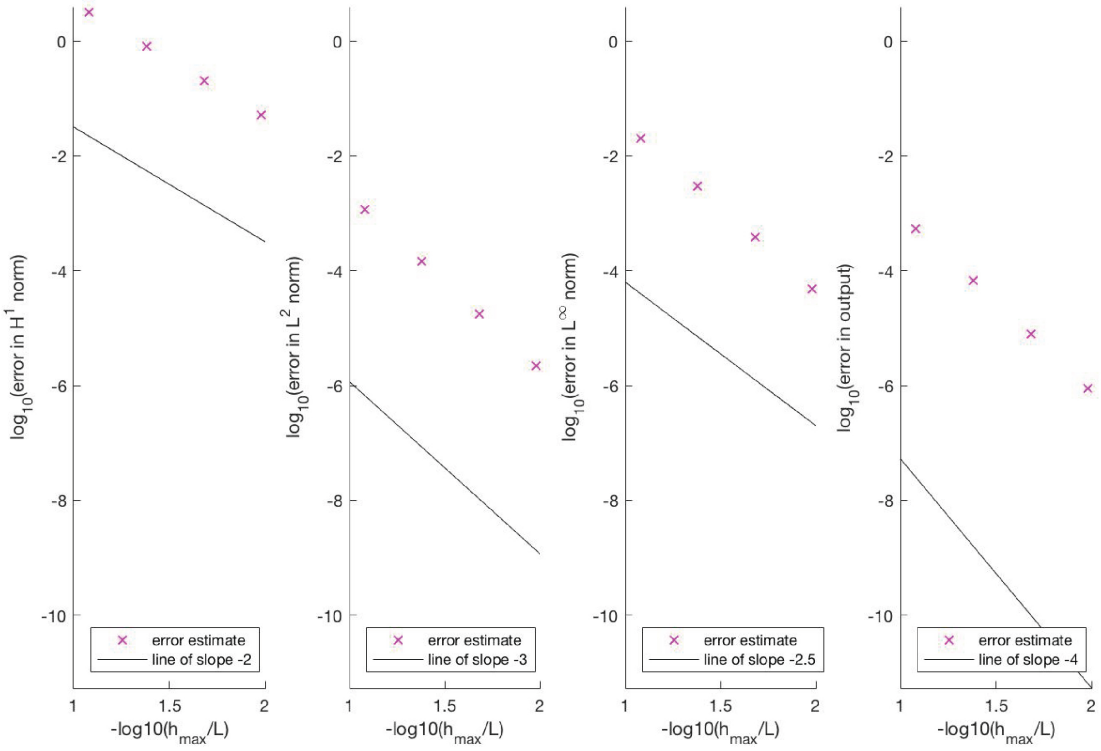

FIGURE 30. Error estimator for $\mathbb{P}_{P=2}$ and $\theta = 0.5$ in $H^1(\Omega)$ norm, $L^2(\Omega)$ norm, $L^\infty(\Omega)$ norm, and the output.

3.4.3. *Indirect Validation.*
To provide confidence that the physical model is sufficiently accurate to provide design guidance we will apply it to a second recipe [2]. In her recipe, Andrea Lott Haney, recommends burger patties of 0.025m thickness and 0.089m diameter, a skillet temperature of $T_{skillet} = 190.56°C$ and cooking times of $t^I = 4$ min, $t^{II} = 3$ min, and $t^{III} = 5$ min.

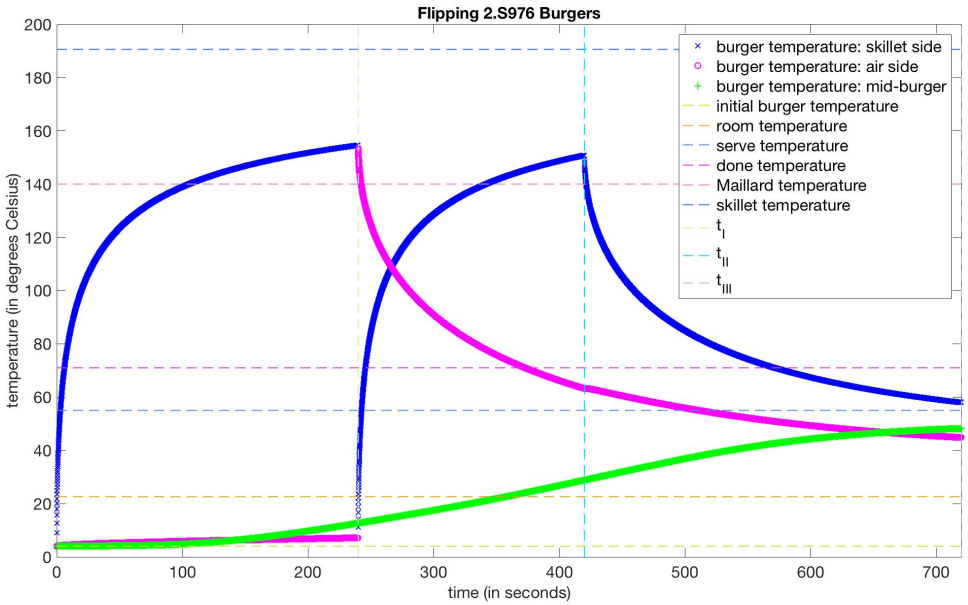

FIGURE 31. Burger temperatures at the skillet side, air side, and in the middle as a function of time.

Retaining the original constraint temperature values, the test recipe [2] allows the burger to reach Maillard temperature, however does not reach a final internal temperature above T_{done} and falls slightly below the ideal serving temperature T_{serve} (Figure 31). However, the original parameters used also failed to bring the internal burger temperature above T_{done} (Figure 28). Because the temperature values are close to prescribed constraints, we cannot assume the model is insufficiently accurate. The discrepancies in T_{done} and T_{serve} are small enough that they could indicate poor choices of constraint temperatures.

4. The FE Method for 1D 4th-Order SPD BVPs

4.1. **Elastodynamics Eigenproblem: Bending.**
For the general problem statement, we consider a beam of length, L, symmetric in both y and z, and with neutral axis $y = 0$. We assume the beam is slender, such that shear stresses are much smaller than normal stresses. The equilibrium equation for our time-dependent, boundary value problem is

$$\frac{d^2}{dx^2}\left(\beta(x)\frac{d^2u}{dx^2}\right) - N_0\frac{d^2u}{dx^2} = q(x,t) - \rho A_{cs}(x)\frac{d^2u}{dt^2}, \tag{1}$$

where $q(x,t)$, is an imposed, time-varying load at position x, N_0 is a constant axial force, and $\beta(x)$ is

$$\beta(x) \equiv (EI)_{eff}(x) \equiv \int_{\mathcal{D}_x} E(x,y,z)y^2 dA. \tag{2}$$

We then consider three possibilities for boundary conditions at both $x = 0$ and $x = L$. For a clamped beam, we assume only essential boundary conditions

$$u(0) = u_{\Gamma_1} \text{ for } x = 0, \tag{3}$$
$$u(L) = u_{\Gamma_2} \text{ for } x = L, \tag{4}$$
$$u_x(0) = u'_{\Gamma_1} \text{ for } x = 0, \tag{5}$$
$$u_x(L) = u'_{\Gamma_2} \text{ for } x = L, \tag{6}$$

where $u(x)$ is the deflection of the beam at x. Likewise, for a free beam, we assumed only natural boundary conditions

$$(\beta u_{xx})_x(0) = -V_{\Gamma_1} \text{ for } x = 0, \tag{7}$$
$$-(\beta u_{xx})_x(L) = V_{\Gamma_2} \text{ for } x = L, \tag{8}$$
$$-\beta(0)u_{xx}(0) = -M_{\Gamma_1} \text{ for } x = 0, \tag{9}$$
$$\beta(L)u_{xx}(L) = M_{\Gamma_2} \text{ for } x = L, \tag{10}$$

where $M(x)$ is the moment applied to the beam and $V(x)$ is the shear force. Finally, we consider a combination of natural and essential boundary conditions for a simply supported beam

$$u(0) = u_{\Gamma_1} \text{ for } x = 0, \tag{11}$$
$$u(L) = u_{\Gamma_2} \text{ for } x = L, \tag{12}$$
$$-\beta(0)u_{xx}(0) = -M_{\Gamma_1} \text{ for } x = 0, \tag{13}$$
$$\beta(L)u_{xx}(L) = M_{\Gamma_2} \text{ for } x = L. \tag{14}$$

For simplicity, we will proceed with homogeneous boundary conditions for a simply supported beam (11-14). The initial conditions are given by

$$\text{displacement: } u(x, t = 0) = u_{ic} \text{ for } x \text{ in } \Omega \tag{15}$$
$$\text{velocity: } \dot{u}(x, t = 0) = \dot{u}_{ic} \text{ for } x \text{ in } \Omega \tag{16}$$

From the modal representation of $u(x,t)$

$$u(x,t) = \sum_{k=1}^{\infty} (c_1^{(k)} \cos w_n^{(k)} t + c_2^{(k)} \sin w_n^{(k)} t) u^{(k)}(x), \tag{17}$$

we can frame our time-dependent boundary value problem as an eigenproblem

$$\frac{d^2}{dt^2} \begin{pmatrix} \cos wt \\ \sin wt \end{pmatrix} = -w^2 \begin{pmatrix} \cos wt \\ \sin wt \end{pmatrix} \text{ where } w^{(k)} = \sqrt{\lambda^{(k)}}. \tag{18}$$

Assuming $q(x,t) = 0$ and substituting (18) into (1) yields the new equilibrium equation

$$\frac{d^2}{dx^2}\left(\beta(x)\frac{d^2u^{(k)}}{dx^2}\right) - N_0\frac{d^2u^{(k)}}{dx^2} = \lambda^{(k)}\rho A_{cs}(x)u^{(k)}. \tag{19}$$

The first order condition for the Rayleigh-Ritz minimization of our eigenproblem becomes

$$\underline{A}\underline{u}_h^{(k)0} = \lambda_h^{(k)}\underline{M}^{inertia}\underline{u}_h^{(k)0}. \tag{20}$$

Matrices $\underline{A}$ and $\underline{M}^{intertia}$ are constructed from $\widetilde{A}_{ij}$ and $\widetilde{F}_i$ where

$$\widetilde{A}_{ij} = \int_0^L \left[\beta(x) \frac{d^2\varphi_i}{dx^2} \frac{d^2\varphi_j}{dx^2} + N_0 \frac{d\varphi_i}{dx} \frac{d\varphi_j}{dx} \right] dx, \tag{21}$$

$$\widetilde{F}_i = \lambda_h^{(k)} \sum_{j=1}^{2\times n_{node}} \int_0^L \rho A_{cs}(x) \varphi_i \varphi_j dx \; u_{hj}^{(k)}, \tag{22}$$

$$\widetilde{M}^{inertia} = \int_0^L \rho A_{cs}(x) \varphi_i \varphi_j dx. \tag{23}$$

Removing rows/columns 1 and $n-1$ from $\widetilde{A}_{ij}$ and $\widetilde{M}^{inertia}$, to account for essential boundary conditions, yields matrices $\underline{A}$ and $\underline{M}^{intertia}$ from (20).

4.2. **Xylophone Bar.**

4.2.1. *Governing Eigenproblem.*

For this problem, we consider a bar of length, L_d, width, and height $H_d(x_d)$ such that

$$H_d(x_d) = \begin{cases} H_{maxd} \left[(1 - P_2) \left(\frac{L_{d/2} - x_d}{L_{d/2} - x_d^*} \right)^{P_1} + P_2 \right] & x_d^* \le x \le L_d - x_d^* \\ H_{maxd} & 0 \le x_d < x_d^* \\ H_{maxd} & L_d - x_d^* < x_d \le L_d \end{cases} \tag{24}$$

where P_1 is an even integer and $P_2 \in [0.05, 1.00]$. We model the Xylophone bar as a free bar with equilibrium equation

$$\frac{d^2}{dx_d^2} \left(\frac{E_d W_d H_d^3(x_d)}{12} \frac{d^2 u_d^{(k)}}{dx_d^2} \right) = \lambda_d^{(k)} \rho_d W_d H_d(x_d) u_d^{(k)}, \tag{25}$$

and boundary conditions

$$u_{dxx}^{(k)} = u_{dxxx}^{(k)} = 0 = u_{dxx}^{(k)}(L_d) = u_{dxxx}^{(k)}(L_d), \tag{26}$$

$$M_d(0) = V_d(0) = 0 = M_d(L_d) = V_d(L_d). \tag{27}$$

Nondimensionalization allows us to rewrite (25) as

$$\frac{d^2}{dx^2} \left(\frac{H^3(x)}{12} \frac{d^2 u^{(k)}}{dx^2} \right) = \lambda^{(k)} H(x) u^{(k)}, \tag{28}$$

with boundary conditions

$$u_{xx}^{(k)} = u_{xxx}^{(k)} = 0 = u_{xx}^{(k)}(1) = u_{xxx}^{(k)}(1), \tag{29}$$

and non-dimensional eigenvalue

$$\lambda^{(k)} = \lambda_d^{(k)} \frac{\rho_d L_d^4}{E_d H_{maxd}^2}. \tag{30}$$

4.2.2. *Design Problem.*
Our design problem is to determine the P_2 and L_d values that yield the desired timbre and pitch. To do this, we select a desired frequency ratio, $R_{target} = \frac{f_d^{(4)}}{f_d^{(3)}}$, where $f_d^{(3)}$ is the fundamental frequency and $f_d^{(4)}$ is the first harmonic. We can then find P_2^{opt} such that

$$\left|R(P_2^{opt}) - R_{target}\right| \leq tol_R \tag{31}$$

where tol_R is our prescribed tolerance for timbre. Now, with P_2^{opt} from timbre optimization, we can determine the length of the bar, L_d, that gives us the desired pitch. To do so, we select a desired fundamental frequency, $f_d^{(3)}$, and find L_d such that

$$\left|f_d^{(3)}(L_d) - f_{targetd}^{(3)}\right| \leq tol_{f^{(3)}} \tag{32}$$

where $tol_{f^{(3)}}$ is our prescribed tolerance for the pitch. Finally, with our optimal values of P_2 and L_d, we can find the optimal positions for the two string holes, x_d^{hole1} and x_d^{hole2} such that

$$u_d^{(3)}(x_d^{hole1}) = u_d^{(3)}(x_d^{hole2}) = 0. \tag{33}$$

4.2.3. *Implementation of Root Finder.*
As described in 4.2.2, the optimal locations for the string holes in the xylophone bar are the positions where the displacement is zero for the fundamental mode. For each hole, we first find the element, m^*, that contains the zero. To do this, the code iterates through each element, from $1 : n_{el}$, and checks if the value of $u_h^{(3)}$ at the left node, times the value of $u_h^{(3)}$ at the right node is less than zero. If it is, it stores the element number in m^*.

```
1 for m = 1:n_el
2     if u3(lg2(1,m))*u3(lg2(3,m)) < 0
3         mstar = m;
```

The function `lg2(1,m)` returns [`lg(1,m), 1`], or the first node and first degree of freedom. Likewise, the function `lg2(3,m)` returns the second node and the first degree of freedom. Using Hermitian approximation, the first degree of freedom is the function, while second is the derivative of the function. After locating the element that contains the zero, to locate the zero we search

$$\sum_{\ell=1}^{4} u_h^{(3)} lg2(\ell, m^*)\hat{S}_{\ell m^*}(\hat{x}^{hole}) \tag{34}$$

over the interval $[0, 1]$ for the value of $\hat{x}^{hole}$ that makes the function (34) zero.

```
1         interval = [0, 1];
2         u3vec = [u3(lg2(1,mstar)), u3(lg2(2,mstar)), ...
              u3(lg2(3,mstar)), u3(lg2(4,mstar))];
3         fun = @(x) u3vec*hshape_fcn(x, h(mstar));
4         xhole = fzero(fun, interval)
```

Finally, we must scale the value of $\hat{x}^{hole}$ to the dimensional domain giving us our desired hole locations, $\hat{x_d}^{hole1}$ and $\hat{x_d}^{hole2}$.

```
1          xhole_d(counter)=(xpts(lg(1,mstar))+h(mstar).*xhole)*L_d;
```

The `counter` variable allows us to store locations of both holes and avoid returning a zero we have already found.

4.2.4. *Verification.*
To verify that the algorithm is performing corrrectly, we plot the modal deflection for the fundamental mode, along with our chosen hole locations, and the bar profile.

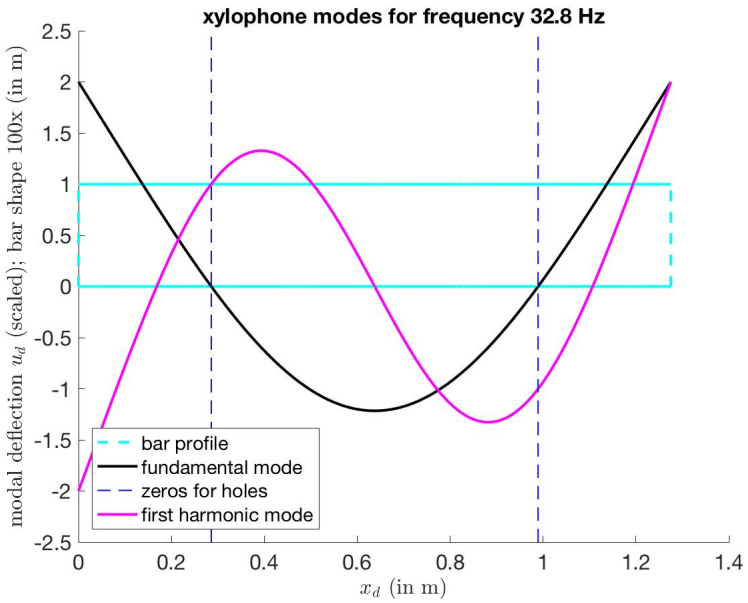

FIGURE 32. The xylophone bar profile, chosen zeros for holes, and modal deflection for the first and fundamental modes

Again, we select hole locations in the xylophone bar such that they coincide with zero deflection for the fundamental mode.

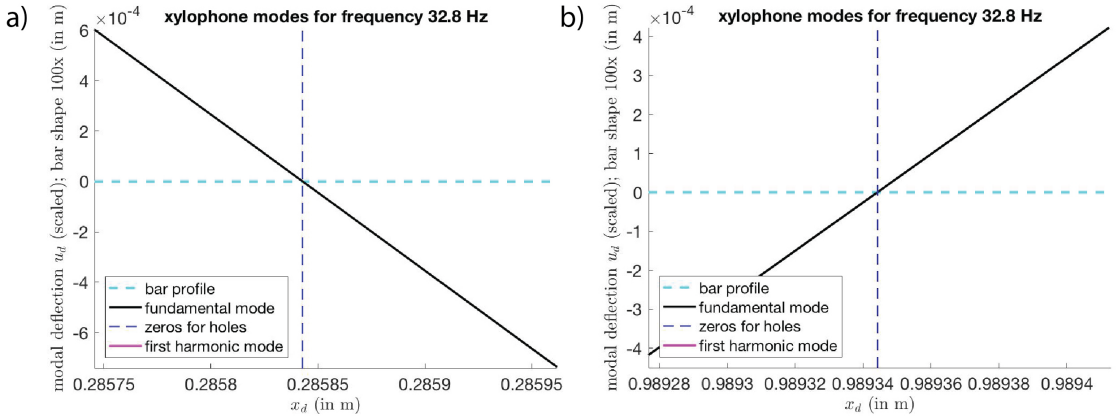

FIGURE 33. Magnification of Figure 32 over the left hole location (a) and right hole location (b)

Examination of the plots (Figure 32, 33) provides evidence that our implementation

is performing correctly. We can see that the vertical lines for hole zeros intersect the modal deflection curves for the fundamental mode at zero (Figure 33ab).

4.3. **Verification, Convergence, and Error Estimators.**

4.3.1. *Mauro Caresta: Vibrations of a Free-Free Beam.*

To provide confidence that our implementation correctly calculates the fundamental and first harmonic frequencies and correctly determines the length L_d required to realize a desired fundamental frequency, we can compare the results of the model to a similar study conducted by Mauro Caresta [3]. Exciting a beam of length $L = 1.275m$, height $h = 0.01$m, $\rho = 7800\text{Kgm}^{-3}$, $E = 2.1 \times 10^{11}\text{Nm}^{-1}$, and $v = 0.3$, Caresta experimentally determined the first five natural frequencies in bending vibration [3]. For the fundamental frequency, he obtained an experimental value of 32.25Hz for a theoretical value of 32.80Hz [3]. Similarly, for the first harmonic frequency, he obtained an experimental value of 88.5Hz for a theoretical value of of 90.44Hz [3].

In his study, Caresta used a beam of uniform cross section. Therefore, we do not optimize for P_2 when we run the model. Using the same parameters as Caresta, our model yields a fundamental frequency of 32.8000Hz with an error estimate of 2.7779×10^{-7}, a first harmonic frequency of 90.4145Hz with an error estimate of 1.0078×10^{-7}, and a length of 1.2752m. Our value for the first harmonic frequency is within 1Hz of Caresta's value. Because this is below the JND value for human hearing, we can say that our model is sufficiently accurate. Similarly, the length outputted by our model differs from Caresta's by less than a millimeter on a beam over a meter in length allowing us to conclude the model is performing correctly.

4.3.2. *Xylophone Bar Tuning.*

We now examine the convergence of our error estimators by testing our model with tuning parameters of pitch F4, or a fundamental frequency of 349.23Hz, and a frequency ratio of 3 ("quint" tuning). The model returns a fundamental frequency value of 349.2300Hz with an error estimate of 5.8496×10^{-6} and a first harmonic frequency of 1044.6Hz with an error estimate of 9.9144×10^{-5}. The values of L_d and P_2 are 0.3264m and 0.6438 respectively, and the hole locations are [0.674 0.2590].

Using the outputs and associated error estimates from our model, with tuning parameters of pitch F4 and a frequency ratio of 3, we can develop an error interval for the frequency ratio, `frequency4_d`/`frequency3_d`. The largest value that the ratio could assume is $\frac{349.2300+5.8496\times10^{-6}}{1044.6-9.9144\times10^{-5}}$. Likewise, the smallest value that the ratio could assume is $\frac{349.2300-5.8496\times10^{-6}}{1044.6+9.9144\times10^{-5}}$. These two values form the upper and lower bounds of our error interval, meaning we can be confident the frequency ratio is within those values.

Examination of the plot of modal deflection for the fundamental and first harmonic mode, the bar profile, and the hole locations provides some initial confidence that our implementation is correct. The hole locations intersect the modal deflection for the fundamental mode at zero, where we expect them to (Figure 34).

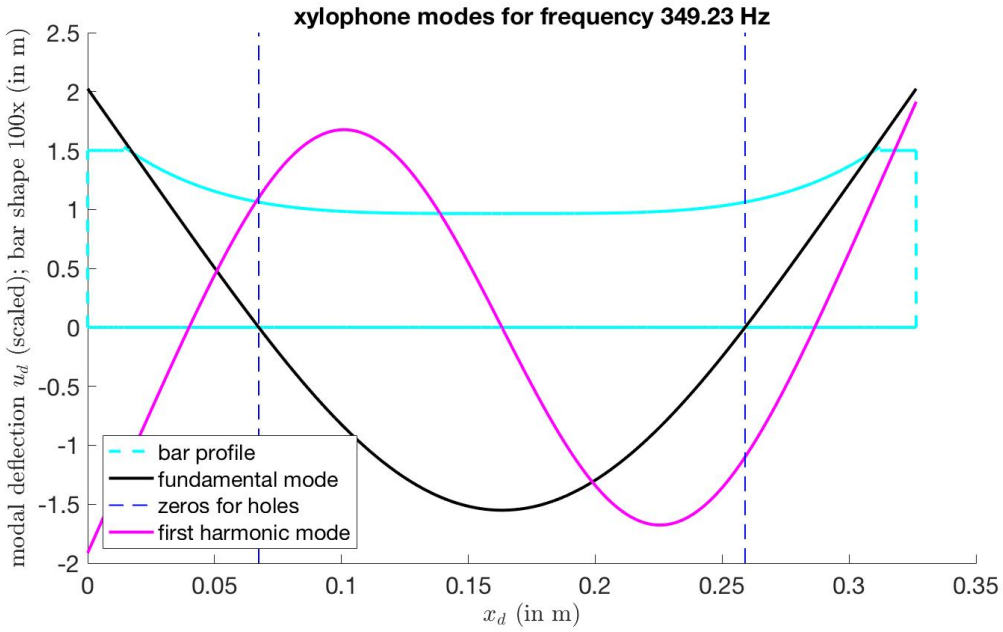

FIGURE 34. The xylophone bar profile, chosen zeros for holes, and modal deflection for the first and fundamental modes

However, we can get further confidence from examination of the convergence plots of error estimators in each norm.

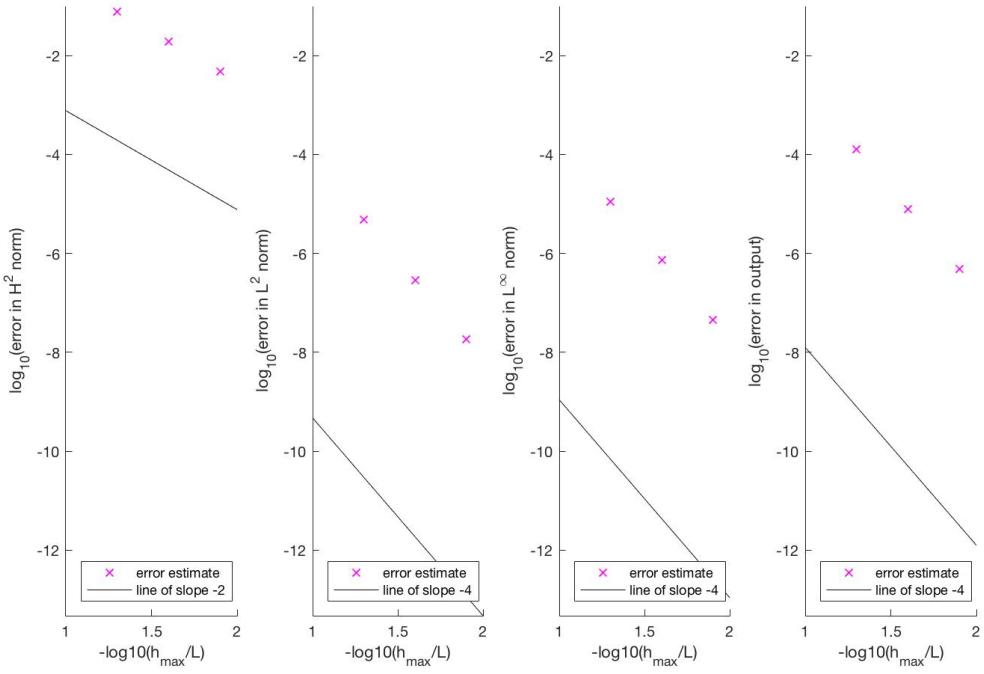

FIGURE 35. Error estimators for the eigenfunctions (fundamental mode) in $H^2(\Omega)$ norm, $L^2(\Omega)$ norm, $L^\infty(\Omega)$ norm, and error estimator for the eigenvalues (fundamental mode) the output.

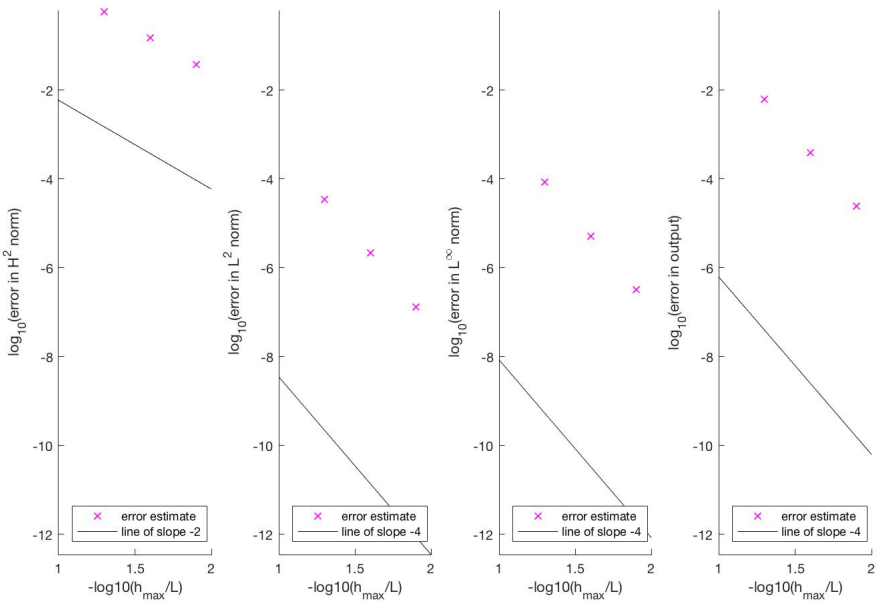

FIGURE 36. Error estimators for the eigenfunctions (first harmonic mode) in $H^2(\Omega)$ norm, $L^2(\Omega)$ norm, $L^\infty(\Omega)$ norm, and error estimator for the eigenvalues (first harmonic mode) the output.

Under the smoothness assumption, for a fixed k the error estimator converges as

$$\left|\left|u^{(k)} - u_h^{(k)}\right|\right|_Q \approx C_{u^{(k)}} h^{r(Q)} \tag{35}$$

where the spatial convergence rates, $r(Q)$, are given by

$$r = \begin{cases} 2 & Q \equiv H^2(\Omega) \\ 4 & Q \equiv L^2(\Omega) \\ 4 & Q \equiv L^\infty(\Omega) \\ 4 & Q \equiv \text{output} \end{cases} \tag{36}$$

For both the fundamental mode and the first harmonic, u_h is converging to u in the $H^2(\Omega)$ norm at the correct rate of 2 (Figures 35a, 36a). Similarly, for the $L^2(\Omega)$ norm, $L^\infty(\Omega)$ norm, and output, u_h is converging to u at the correct rate of 4 (Figures 35bcd, 36bcd). Convergence at the correct rates provides additional confidence that our implementation is correct.

Running the model a second time, with tuning parameters of pitch C5, or a fundamental frequency of 523.25Hz, and a frequency ratio of 3 ("quint" tuning) yields a fundamental frequency value of 523.2500Hz with an error estimate of 8.7645×10^{-6} and a first harmonic frequency of 1565.2Hz with an error estimate of 1.4855×10^{-4}. The values of L_d and P_2 are 0.2667m and 0.6438 respectively, and the hole locations are [0.0551 0.2116].

For the same mesh, the FE error should be larger for `frequency4_d` than it is for `frequency3_d`. This is because we only have a finite number of eigenvalues, n,

and to capture higher modes you need higher resolution. The model results support this claim. In the first case, for pitch F4, the error estimate for `frequency4_d` was 9.9144×10^{-5} and for `frequency3_d` was 5.8496×10^{-6}. The second case, for pitch C5, also confirms this. For pitch C5, the error estimate for `frequency4_d` was 1.4855×10^{-4} and for `frequency3_d` was 8.7645×10^{-6}. Provided that the sensitivity of the untrained human ear is roughly 10Hz, error estimates on the order of 10^{-4} to 10^{-6} are very small. This indicates that we could use a coarser mesh because, given human sensitivity, the precision we have is not necessary.

Outside of implementation and FEM errors, we also introduce modeling errors from our treatment of the xylophone bar as an Euler-Bernoulli beam. In Euler-Bernoulli beam theory, we neglect rotary inertia and shear deformation. However, for high-order modal frequencies both rotary inertia and shear deformation have large effects on vibration behavior. Therefore, our predictions will be more accurate for bars tuned to low-frequencies than for bars tuned to high frequencies.

4.4. **Model I: Introduction of "Robin" Boundary Condition.**

We now consider a beam of length L with a lumped (massless) Hookean spring attached to the right end. The boundary conditions at the left end are now, $u_{xx} = u_{xxx} = 0$, and at the right end are $u_{xx} = 0$ and $-(EIu_{xx})_x = -k_s u$ where k_S is the positive spring constant. To add this "Robin" boundary condition, we only need to add a term, $\frac{1}{2}k_s w^2(L)$, to our energy functional. The stiffness matrix then becomes

$$A_{ij} = \int_0^L EI \frac{d^2\psi_i}{dx^2}\frac{d^2\psi_j}{dx^2}dx + k_S\psi_i(L)\psi_j(L) \tag{37}$$

To implement this, in `impose_boundary_cond.m` we select the first degree of freedom of the right most node with the function, `ttomap_fcn(n_el+1,1)`. Then we simply modify our A matrix at position `A(rightside_node,rightside_node)` by adding in our spring constant term.

```
gam_Gamma2 = probdef.gam_Gamma2;
rightside_node = ttomap_fcn(n_el0+1,1);
if(Dir(1,2) == true)
    bEnodes = [bEnodes,rightside_node];
    uDir = [uDir,u_Gamma2(1)];
    n = n - 1;
else
    F(rightside_node) = F(rightside_node) + f_Gamma2(1);
    A(rightside_node) = A(rightside_node, rightside_node) + ...
        gam_Gamma2(1);
end
```

In `library_of_models.m` we add a problem definition for `gam_Gamma2` such that the value for the first degree of freedom is $-k_S$, our spring constant.

```
ks = param.ks;
probdef.gam_Gamma2 = [-ks; 0];
```

5. The FE Method: Self-Buckling

Buckling Eigenproblems

Sarah Bardin, May 16th 2019

2.S976 Finite Element Methods for MechE

Self-Buckling

Eigenproblem:

$$\frac{d^2}{dx^2}\left(R^4\frac{d^2u}{dx^2}\right) = \lambda\left(\frac{d}{dx}\left(P\frac{du}{dx}\right)\right)$$

$$u = u_x = 0 \text{ at } x = 0$$

$$u_{xx} = (R^4 u_{xx})_x = 0 \text{ at } x = 1$$

and normalization of u

$\lambda^{(1)} = \gamma_c$ Critical Load Parameter

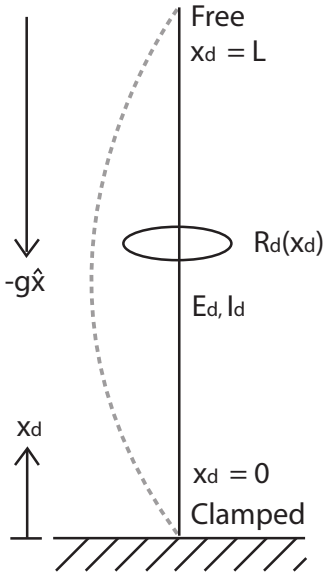

No self-buckling for:

$$\gamma = \frac{4\pi\rho g L_d^4}{E_d V_d} < \lambda_c$$

FE Methods for Self-Buckling

Discrete Equations (first mode):

$$\underline{A}\underline{u}_h^0 = \lambda_h \underline{K}^{ax} \underline{u}_h^0$$

$$\underline{u}_h = [0; 0; \underline{u}_h^0]$$

$$\widetilde{A}_{ij} = A_{ij}^N = \int_0^1 R^4(x) \frac{d^2\varphi_i}{dx^2} \frac{d^2\varphi_j}{dx^2} dx$$

$\underline{A} = \underline{\widetilde{A}}$ with rows and columns 1 and 2 removed

$$\widetilde{K}_{ij}^{ax} = K_{ij}^{axN} = \int_0^1 P(x) \frac{d\varphi_i}{dx} \frac{d\varphi_j}{dx} dx$$

$\underline{K}^{ax} = \underline{\widetilde{K}}^{ax}$ with rows and columns 1 and 2 removed

Optimization Problem

Radius Function: $R(x) = \sqrt{1 + G(x)}$

Parameterization:

$$G^{\text{shape family}}(x, p_1(\text{our design variable}), p_2, ...)$$

Design Constraints:

1) Fixed Volume: $\int_0^L G(x)dx = 0$
2) Minimum Radius: $G(x) \geq -1 + R_{min}^2$
3) Gradual Variation: $|G'(x)| \leq S_{max}$

Optimization Problem

Objective:

Maximize L_d subject to CV (1), CM (2), CS (3)

1. maximize γ_c over $p_1 : \gamma_c^{opt}$
2. choose $L_d^{opt} = \left(\frac{\gamma_c^{opt} E_d V_d}{4\pi\rho g}\right)^{1/4}$

Figure of Merit:

$$\frac{L_d^{opt}}{L_{d,cyl}^{opt}}(\text{at fixed volume}) = \left(\frac{\gamma_c^{opt}}{\gamma_{c,cyl}^{opt}}\right)^{1/4}$$

Column Design: FOM=1.644

$$G(x) = -0.96 \sin\left(\pi(x - 0.5)\right)$$

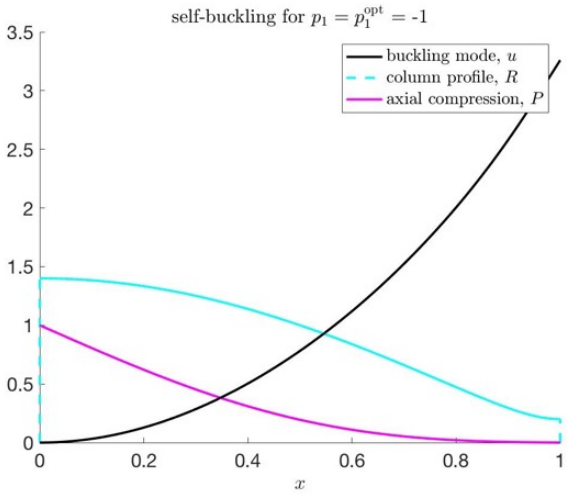

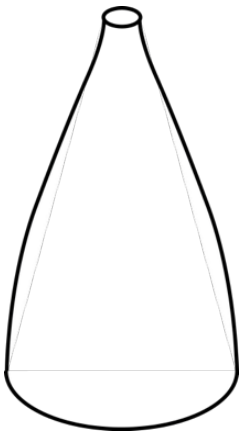

Column Design:

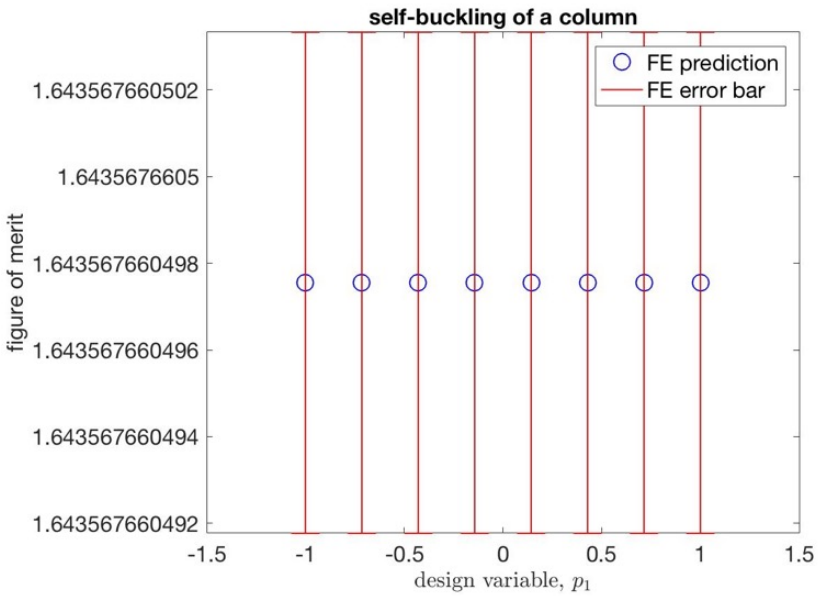

Column Design: Constraint Satisfaction

$$G(x) = -0.96 \sin(\pi(x - 0.5))$$

1) Fixed Volume: $\int_0^L G(x)dx = 0$

2) Minimum Radius: $G(x) \geq -1 + R_{min}^2 = -0.96$

$$G(0) = -0.96 \sin(\pi(-0.5)) = -0.96$$

3) Gradual Variation: $|G'(x)| \leq S_{max} = 10$

$$|G'(x)| = 3.0159 \leq 10$$

FE Error

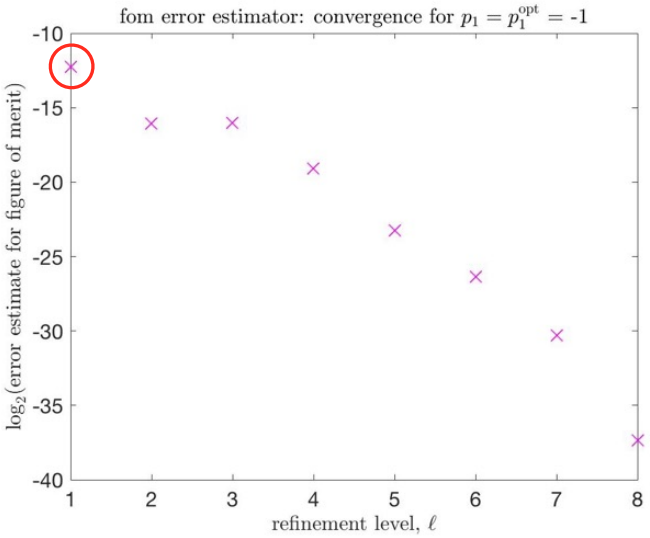

Error Estimate

$$= 2^{-12.26}$$
$$= 0.00020 < 0.01$$ ✓

Convergence

A Priori Estimate

$$\lambda_h - \lambda \sim C_u \left(\frac{h}{h_0}\right)^4$$

A Posteriori Estimate

$$\log_2 \Delta_h^{\lambda}(\ell) \sim \log_2 C_u - 4\ell$$

References

[1] Patera, A. *Finite Element Methods and Related Variational Techniques for Numerical Approximation of PDEs*; Massachusetts Institute of Technology, 2018.
[2] Haney, AL. *How to Cook Hamburger on an Electric Griddle* https://www.leaf.tv/articles/how-to-cook-hamburger-on-an-electric-griddle/
[3] Caresta, Mauro. *Vibrations of a Free Beam* http://www.varg.unsw.edu.au/Assets/link20pdfs/Beam_vibration.pdf

2.S976 Finite Element Methods for Mechanical Engineers, Massachusetts Institute of Technology, Department of Mechanical Engineering, Cambridge MA 02139